Biomaterials Advances 179 (2026) 214523

Contents lists available at ScienceDirect

Biomaterials Advances

journal homepage: www.journals.elsevier.com/materials-science-and-engineering-c

Implementation of a fully biodegradable and biomimetic epicardial patch providing synergic physico-chemical, mechanical and electrical cues for myocardial infarction therapy

Caterina Cristallini [a,b,*], Daniela Rossin [c,**], Niccoletta Barbani [b,a], Roberto Vanni [c], Massimiliano Labardi [a], Cheherazade Trouki [a,d], Silvia Burchielli [e], Claudia Kusmic [f], Domiziana Terlizzi [e], Francesca Sergi [b], Chiara Bulgheresi [b], Dawid Rossino [a,b], Erika Fiorino [c], Matteo Aubry [c], Marco Lo Iacono [c], Sadia Perveen [c], Giorgia Scarpellino [g,1], Luca Munaron [g,h], Sara Amorim [i,j], Ricardo A. Pires [i,j], Rui L. Reis [i,j], Raffaella Rastaldo [c,2], Claudia Giachino [c,2]

[a] Institute for Chemical and Physical Processes, CNR-IPCF, via Giuseppe Moruzzi 1, 56124, Pisa, Italy
[b] Department of Civil and Industrial Engineering, DICI, University of Pisa, Largo Lucio Lazzarino, 56126, Pisa, Italy
[c] Department of Clinical and Biological Sciences, University of Turin, Regione Gonzole 10, 10043, Orbassano, Italy
[d] Department of Pharmacy, University of Pisa, via Bonanno 6, 56126, Pisa, Italy
[e] Fondazione Monasterio, via Giuseppe Moruzzi 1, 56124, Pisa, Italy
[f] Clinical Physiology Institute, CNR-IFC, via Giuseppe Moruzzi 1, 56124, Pisa, Italy
[g] Department of Life Sciences and Systems Biology, University of Turin, Via Accademia Albertina 13, 10123, Torino, Italy
[h] Nanomaterials for Industry and Sustainability Inter-Departmental Centre (NIS), University of Turin, Italy
[i] 3B's Research Group, I3Bs - Research Institute on Biomaterials, Biodegradables and Biomimetics, University of Minho, Headquarters of the European Institute of Excellence on Tissue Engineering and Regenerative Medicine, AvePark, Parque de Ciência e Tecnologia, Zona Industrial da Gandra, 4805-017, Barco, Guimarães, Portugal
[j] ICVS/3B's-PT Government Associate Laboratory, Braga, Guimarães, Portugal

ARTICLE INFO

Keywords:
Acellular bioartificial scaffold
Electrical conductivity
Cardiac tissue biomimicry
Biodegradability
Myocardial infarction

ABSTRACT

The intrinsic limitation of myocardial tissue to self-repair after damage underscores the need for innovative approaches in addressing cardiac tissue damage post-myocardial infarction (MI). We aimed to develop an acellular, bioartificial, microstructured and electroconductive patch (PGF) made of poly(lactic-*co*-glycolic acid) (PLGA), Gelatin, and 9-fluorenylmethoxycarbonyl-diphenylalanine (Fmoc-FF), to foster post-MI endogenous cardiac healing capabilities. The self-assembling semi-conductive peptide Fmoc-FF was introduced to reduce the electrical impedance of the polymer components while maintaining the complete biodegradation of the patch. Unexpectedly, the electroconductive component was found to increase the patch microstructure stability, improve cardiomyoblast elongation, augment stromal cell differentiation and sustain Human induced Pluripotent Stem Cell-derived Cardiomyocytes (hiPSC-CM) beating for at least 30 days. The main outcome was demonstrated *in vivo*, where epicardial implantation of the PGF patch in a rat model of ischaemia-reperfusion promoted significant cardiac tissue repair: this was evidenced by preservation of the myocardial tissue, reduced fibrosis, and recruitment of endogenous c-Kit+ cells. This newly implemented patch configuration promotes efficient myocardial healing, offering a promising therapeutic approach for infarcted patients.

* Corresponding author at: Institute for Chemical and Physical Processes, CNR-IPCF, via Giuseppe Moruzzi 1, 56124, Pisa, Italy.
** Corresponding author.
E-mail addresses: caterina.cristallini@cnr.it (C. Cristallini), d.rossin@unito.it (D. Rossin).
[1] Present address: Department of Biology and Biotechnology "L. Spallanzani", University of Pavia, *Via* Adolfo Ferrata 9, 27100 Pavia, Italy.
[2] These Authors contributed equally to the work.

https://doi.org/10.1016/j.bioadv.2025.214523
Received 2 April 2025; Received in revised form 4 September 2025; Accepted 21 September 2025
Available online 24 September 2025
2772-9508/© 2025 The Authors. Published by Elsevier B.V. This is an open access article under the CC BY license (http://creativecommons.org/licenses/by/4.0/).

1. Introduction

The reduced intrinsic capacity of myocardial tissue to self-repair after damage is the main cause of the formation of irreversible tissue scarring and subsequent impairment of cardiac function [1]. Current therapies for myocardial infarction (MI) are focused on symptom management rather than addressing long-term damage to heart tissue, which can progressively lead to heart failure [2,3].

Acknowledging the limitations associated with existing treatments, the development of strategies aimed at promoting the innate but limited cardiac healing capacity emerged as a crucial approach for addressing the rising population of heart disease patients [4]. In this context, cardiac tissue engineering (TE) offers a promising avenue through the development of 3D scaffolds, like cardiac patches [5,6], which are designed to be placed on the heart's surface to support the damaged tissue. Historically, all 3D cardiac patches in clinical studies have been implanted *via* open-chest cardiac surgery, often during procedures like coronary artery bypass grafting, which remains the only established surgical approach. However, recent advances have demonstrated the technical feasibility of robotic, minimally invasive, cardiac patch implantation in a porcine cadaver model [7], representing a promising step toward less invasive delivery methods. Regardless of the implantation method, the goal of cardiac TE is to replace the damaged extracellular matrix (ECM) by using a biodegradable scaffold that can provide all the necessary topographical, biochemical, and mechanical cues. This creates an optimal microenvironment for cell adhesion, diffusion, proliferation, and differentiation, closely mimicking the natural properties of the native cardiac ECM [8–11]. In the past few years, aliphatic polyesters (*e.g.*, polyglycolic acid (PGA), polycaprolactone (PCL), poly(lactic-co-glycolic acid) (PLGA), polyurethanes (PU), poly(glycerol sebacate) (PGS) and natural polymers (*e.g.* collagen, gelatin, alginate, chitosan, fibrinogen) have been considered in cardiac TE [12]. The combination of synthetic and natural polymers (named bioartificial polymeric materials) was demonstrated to be an excellent strategy to match the best properties of both, providing an excellent candidate as a cardiac patch exhibiting biocompatibility, mechanical performance and biodegradability [13]. Importantly, a suitable material composition can be associated with tailored topographical design features typical of an anisotropic myocardium structure. Indeed, various technologies (*e.g.* soft lithography and electrospinning) have been developed to engineer patches bearing relevant mechanical and structural signals to promote cardiomyocyte alignment and function [14,15]. In previous studies, we have demonstrated how microstructured PG acellular patches mimicking the cardiac ECM effectively favour adhesion, long-term viability, differentiation and orderly disposition of cardiac-relevant seeded cells, as well as provide cardioprotection in a large animal model [16,17].

Controlling the biodegradability of artificial structures is crucial for effective healing, allowing integration with the endogenous ECM and gradual replacement by natural tissue. Additionally, the material's conductivity is crucial for synchronizing cell beating, enhancing cardiomyocyte coupling, and boosting cardiac marker expression [18]. Synthetic and natural polymers, commonly used in the production of scaffolds for TE, including cardiac patches, lack electrical conductivity. For this reason, the category of electrically conductive polymers (CPs), including polyaniline, polypyrrole, polythiophene, as well as polymer composites comprising conductive nanoparticles, such as graphene, gold, or carbon nanotubes (CNTs), has recently received significant attention as biomaterials [19–22]. However, the suitable electrical properties of CPs are not combined with adequate biocompatibility, processability and fabrication methods. To solve this issue, in the last two decades, many *in vitro* and some *in vivo* studies focused on strategies of blending, copolymerization, interpenetrating polymer networks (IPNs), and hydrogels conjugation of CPs into biodegradable synthetic or biological polymers [23].

Recent advancements in electroconductive biomaterials aim to better replicate the conductivity of native cardiac tissue, potentially improving signal propagation across fibrotic tissue after MI and supporting stem cell differentiation [18,24–28]. Among these, conducting polymer-based hydrogels have attracted significant interest for their potential to induce cardiac tissue regeneration [28–30]. These materials are typically employed through two primary strategies: direct injection or epicardial application. Some hydrogels are designed to be injected into the myocardium, offering a minimally invasive delivery method. While this approach is promising, injectable hydrogels often lack the mechanical strength required to provide structural support to the damaged ventricular wall, a critical aspect of post-infarction therapy. In contrast, cardiac patches, which can be fabricated from various materials including conductive hydrogels, are applied directly to the epicardium. Epicardial therapies, based on passive or adhesive approaches active devices, are increasingly considered as promising strategies for MI treatment [14]. A recent example of innovation in this area is a functionalized polyaniline-polyvinyl alcohol adhesive hydrogel patch was developed, allowing a conformable integration with the epicardial surface for simultaneous diagnosis and myocardial tissue regeneration [31]. However, one of the main restrictions in the extensive use of conducting materials is their intrinsic non-degradability [32]. In most studies, the followed approach is to combine ECs with synthetic or biological biodegradable polymers, but this does not allow complete biodegradation. Moreover, the synthesis of degradable and conducting polymers containing conducting oligomers is widely explored; however, it still represents a challenge [33]. To address this issue, our interest focused on the use of Fmoc-FF, a conductive amphiphilic peptide that can enhance the electrical properties of the patch while maintaining optimal biocompatibility and biodegradability [34]. The low molecular weight hydrogel composed of Fmoc-FF, known for its capacity to form hydrogels under physiological conditions without requiring cross-linking agents, has been widely studied for diverse biomedical applications since its discovery in 2006 [34–36]. The use of this peptide offers several advantages, including the ability to mimic the chemical composition and bioactivity of ECM proteins because of its peptide nature [37], and to biodegrade in physiological conditions; the capacity to promote stem cell differentiation into specific lineages (dependent on the storage modulus of the hydrogels) [38,39]; the ability to promote the conductivity, as observed in a series of human tissues, alignment of nanofibers and adaptability to generate micropatterns able to promote cellular alignment [40–42].

We first investigated the method of introducing Fmoc-FF peptide to prepare a cytocompatible, biodegradable, microstructured and electroconductive 3D cardiac patch (PGF). To achieve a homogenous electrical conductivity within the patch, Fmoc-FF was incorporated both in the microstructured external layers and in the inner hydrogel. A wide series of *in vitro* characterizations were performed to evaluate the surface and physicochemical properties, mechanical and degradation performance and conductivity of PGF. Different relevant cell types were seeded on the PGF to evaluate the patch cytocompatibility, cell adhesion, alignment and calcium handling. Finally, the PGF was sutured onto the epicardium of infarcted rat hearts to assess its impact on tissue structure, cardiac protein profile, *in vivo* cell recruitment and fibrosis, through histological, immunofluorescence and chemical imaging studies. Our final aim was to gain a deeper understanding of the impact of our newly implemented epicardial patch in mitigating cardiac damage following MI.

2. Materials and methods

2.1. Materials for patch preparation

Poly(DL-lactide-*co*-glycolide) (PLGA, ratio of lactide to glycolide = 50:50, Mw = 40-75 kDa), gelatin (type A), phosphate-buffered saline (PBS), matrix metalloproteinase-9 human recombinant (MMP-9), were supplied by Sigma-Aldrich (Italy). N-fluorenylmethoxycarbonyl-diphenylalanine peptide (Fmoc-FF), was provided by Biogelx Ltd. (UK). Fmoc-

glucosamine-6 sulfate (Fmoc-GlcS) and Fmoc-glucosamine-6 phosphate (Fmoc-GlcP) were synthesised according to previously established procedures by chemical conjugation of the sugar moiety (Carbosynth, UK) to Fmoc-chloride (Sigma-Aldrich, Germany) [38]. Dichloromethane (DCM), bidistilled water, acetone (ACT), tetrahydrofuran (THF), and ethanol (EtOH) were supplied by Carlo Erba Reagenti (Italy).

2.2. Preparation of m-PG, m-PGF, PG, PGF

Monolayer PLGA/Gelatin patches (m-PG) were prepared using PDMS molds having a myocardial biomimetic micropatterning according to a method already reported [16]. The topological model derived from histological analysis images enabled the achievement of a geometry containing cavities of 500 μm × 100 μm, having dimensions of cell bundles and lines of 30 μm and 70 μm in width, reproducing ECM thickness surrounding cell bundles [16]. Briefly, blends of PLGA and gelatin (70/30 *w*/w) in a ternary solvent (DCM, bidistilled water, ACT at 45 % *v*/v, 19 % v/v and 36 % v/v, respectively) were deposited in PDMS molds. A slow evaporation of the solvent mixture was then allowed by covering the filled molds with porous aluminium masks and leaving them under a chemical fume hood at room temperature for 24 h, as illustrated in Fig. S1. Microstructured PGF monolayers (m-PGF) were analogously prepared by adding Fmoc-FF at 0.025 % (*w/v*) in ACT. Hydrogels based on Fmoc-FF and its co-assembled Fmoc-FF/Fmoc-GlcS and Fmoc-FF/Fmoc-GlcP mixtures in bidistilled water for a final concentration of 10 mM were prepared by their self-assembly promoted by the pH change from pH 12 to around pH 7.5–8.5, followed by sonication for 15 min and cooling at 4 °C for 24 h. Bilayer constructs (PG and PGF, Fig. 3A) were prepared by assembling, on the non-microstructured surface of one of the two layers, two m-PG or m-PGF, leaving the micropatterning outside and depositing 1 mL of gelatin or Fmoc-FF hydrogels, respectively, as shown in Fig. S2. The edges of each bilayer were fixed by die casting at 50 °C (Fig. S2). m-PG and PG were used as controls for m-PGF and PGF.

2.3. Characterization

Selected areas of sample surfaces of 1 mm × 1 mm were analysed by FT-IR Chemical Imaging (Perkin Elmer Spotlight 300, Shelton, CT, USA) and identified employing the optical microscope. Using the ATR objective, the generated spectra were collected, and chemical maps were produced, using micro-ATR mode. The maps were elaborated using the software of the instrument to obtain a correlation map in order to identify the average spectrum, which is the most representative spectrum of the chemical map. Spectra were recorded in the mid-infrared region (4000–750 cm^{-1}) at 16 scans per pixel; the spectral resolution was 4 cm^{-1} and the spatial resolution was 100 × 100 μm. The spectra were also subjected to a Savitzky Golay smoothing procedure (9 points). The data analysis was performed using Principal Component Analysis (PCA), a method for the analysis of large spectral data sets. It represents the spectra in data groupings of similar multi-parameter variability (score) and allows the identification and differentiation of dissimilar spectral groups.

Dynamic mechanical analysis was performed by DMA (DMA8000, Perkin Elmer, USA), using strain scan analysis at 1, 2, and 3 Hz frequencies. Storage modulus (E′), loss modulus (E″) and damping factor (tanδ) were evaluated in dry and wet conditions at 37 °C, applying the strain in parallel and perpendicular directions. Tensile tests were performed by INSTRON (model 5500R- 1185 825, USA) equipped with a 100 N load cell. Sample morphology was characterized by scanning electron microscopy (SEM, FEI QuantaTM 450 FEG Instrument, USA). SEM analysis was done at 10 kV in high-vacuum mode, with manual aperture, 3 beam spot size, at 200–2000 magnification.

Degradation tests of samples in PBS containing MMP-9 (20 ng/mL), to simulate cardiac microenvironment, were performed by gel permeation chromatography (GPC, Perkin Elmer, USA), equipped by a ResiPore (Agilent Technologies, USA) column, using UV and RI detectors, THF as mobile phase, flow at 1 mL•min^{-1}, injection volume of 100 μL, wavelength set at 245 nm.

Conductivity analysis on the samples was carried out using a broadband dielectric spectrometer (Alpha analyzer, Novocontrol GmbH, Darmstadt, Germany). Pre-swelled samples were surrounded by a Teflon ring (diameter 8.5 mm, height 1.3 mm) and covered by two metallic plates serving as the electrodes. The measurement started 30 min after sample placement, once the swelling stability of the patch sample in bidistilled water was achieved. After each measurement, a second one was performed to verify that no changes occurred due to possible water evaporation.

2.4. Cell cultures

H9C2 cardiomyoblasts (ATCC, USA) and human mesenchymal stem cells (hMSCs) (Lonza, Switzerland) were cultured as described in previous works [13,43]. The Cardiomyocytes derived from Human induced Pluripotent Stem Cells (hiPSC-CMs, PluriCell Biotech now LizarBio, Brazil) were cultured in RPMI (Thermo Fisher, Italy) supplemented with 1× B27, 1 % kanamycin and 10 μM rock inhibitor (Sigma-Aldrich, Italy). hiPSC-CMs beating was recorded by using the Motic AE 2000 inverted microscope and elaborated with Motic Images Plus 3.4 Software (Motic, Canada). hiPSC-CMs were seeded 8 × 10^4 cell/cm^2 on 96-well flat-bottom plates, glass coverslips, or patches depending on the experiment, previously coated with Fibronectin (50 μg/mL, Sigma-Aldrich, Italy) to facilitate cell adhesion.

2.5. Biocompatibility of the scaffolds

The m-PG, m-PGF, and PGF biocompatibility was tested using a Propidium Iodide (PI) Flow Cytometry assay as described in a previous work [13]. In brief, H9C2 cells (3 × 10^4 cells) or hMSCs (2 × 10^4 cells) were cultured with the patches, while control cells were cultured alone in cell culture flasks/dishes. After 24, 48 or 72 h, the cells were detached with Trypsin-0.2 % EDTA, resuspended in 500 μL of cold 1× PBS (Sigma-Aldrich, Italy), and transferred into falcon tubes for flow cytometry analysis. Then, 10 μL of PI (1:20 in bidistilled water, Sigma-Aldrich, Italy) were added; after 5 min, cell viability was investigated with CyAN ADP flow cytometer (Beckman Coulter, Brea, CA, USA) and analysed by Summit 4.3 software.

2.6. Cell morphology and elongation analysis

To evaluate cell elongation on patches, H9C2 cells (2,5 × 10^5) were stained with Calcein-AM (1:1000, Sigma-Aldrich, Italy) after 3, 5 or 7 days from seeding. Cell elongation was estimated using “line” and “scale bar” functions from the ZEN 3.4 software (Carl Zeiss Laser Scanning System LSM 510, Germany), applied to 50 cells per each condition. The measured values of cell elongation were then normalized to the 2D control.

To analyze H9C2 cells' morphology on PGF, they were fixed with 4 % PAF (Sigma-Aldrich, Italy) for 30 min, before permeabilizing with 0.1 % Triton X-100 for 15 min and blocking with 6 % BSA (Sigma-Aldrich, Italy) and 2.5 % normal goat serum (NGS, Sigma-Aldrich, Italy) for 1 h. Actin filaments were stained with Tritc-phalloidin for 2 h at RT (Sigma-Aldrich, Italy), and nuclei were counterstained with DAPI (Sigma-Aldrich, Italy) for 30 min. After mounting with Mowiol (Calbiochem, San Diego, CA, USA), images were acquired using ZEN 3.4 software (Carl Zeiss; Laser Scanning System LSM 510, Germany) with a 40× objective.

2.7. RNA extraction and qRT-PCR

hMSCs seeded on m-PG and m-PGF, alongside 2D controls cultured in T75 flasks, were lysed by using Trizol (Sigma-Aldrich, Italy) according to the manufacturer's instructions, and RNA was quantified with

NanoDrop™ ND-1000 spectrophotometer (Euroclone, Italy). cDNA synthesis and qRT-PCR were performed as described in a previous work [13]. Expression levels of target and reference genes (see Table S1) were evaluated with SYBR green technology on an ABI PRISM 7500 Fast Real-Time PCR system (Thermo Fisher, Italy). Melting curve analysis was performed for all amplicons. For each target gene, fold change in expression levels between cellularized scaffolds and 2D controls was evaluated with the $2^{-\Delta\Delta Ct}$ method using UBC as a reference gene and matched 2D controls as calibrators.

2.8. Calcium imaging

hiPSC-CMs cultured on PGF in control conditions for 24 h were loaded with 5 μM Fura-2 AM ratiometric calcium probe (Invitrogen, CA, USA) and, after 30-min incubation (37 °C, 5 % CO_2), the fluorescent signal was acquired using a Nikon Eclipse TE-2000S (Minato, Japan) inverted microscope and Metafluor Imaging System (Molecular Devices, CA, USA). Excitation wavelengths of 340 nm and 380 nm were applied alternatively, and the intracellular calcium concentration ($[Ca^{2+}]_i$) was expressed as the ratio (R) of the fluorescence at 510 nm corresponding to the two excitation wavelengths. For each experimental condition, a minimum of three independent experiments were conducted by selecting at least 20 regions of interest (ROIs) per experiment. During each run, images were background-subtracted and acquired every 500 milliseconds for a minimum of 15 min. The initial 750 s of each time course were analysed using the GNU Octave script available at gist.github.com/Feat-FeAR/ceedb42bd27d67601afe681cd0dea43c. To statistically compare the behaviour of hiPSC-CMs cultured on the different substrates, calcium dynamics were quantitatively characterized in each condition by evaluating basal R levels and spike amplitude in terms of both per-experiment mean value and intercellular variability. Finally, the time-averaged calcium spiking rate and inter-spike interval (ISI) variability were also assessed.

2.9. Experimental design and in vivo validation

The *in vivo* experimental work was conducted on 12 Male Wistar rats (4 months old, 260–426 g body weight) at the Centre for Experimental Biomedicine (CBS), within the CNR Research Area of Pisa, Italy, following approval number 536/2020-PR dated 27/05/2020 issued by the Italian Ministry of Health. All surgery was performed under anaesthesia (Zoletil® at 40 mg/kg, Xylazine at 7.5 mg/kg), pre-emptive analgesic medication (Carprofen at 5 mg/kg), and all efforts were made to minimize suffering. Myocardial ischemia/reperfusion (I/R) was produced by 30 min ligation of the left descending coronary artery (LAD) followed by reperfusion using a technique described in detail in a previous work [44]. The animals were randomly divided into three experimental groups. In the Sham group, rats underwent thoracotomy without LAD ligation. The I/R group underwent thoracotomy and I/R procedure. The I/R + PGF group underwent the same procedure but with epicardial placement of the patch to cover the infarcted area, 10 min after LAD occlusion, sutured with a single detached stitch.

During the post-operative phase, electrocardiographic examinations were carried out following gas anaesthesia (isoflurane 1–2 % in 100 % O_2) administered *via* a mask during spontaneous breath every week until animal sacrifice.

At 4 weeks from surgery, euthanasia was conducted ethically, subjecting the animals to terminal anaesthesia, to ensure that the heart continued to beat during the removal process. After rinsing the harvested hearts in ice-cold saline solution, they were dissected to obtain two ventricular cups. Tissue samples were fixed in 10 % buffered formalin for 48–72 h to facilitate histopathological examination. Samples underwent dehydration, xylene clearing, and embedding in paraffin wax with a melting point of 56 °C. Subsequent transversal sections of the heart (thickness = 5 μm) were cut, placed onto slides, and allowed to dry overnight at 40 °C.

2.10. Histology and immunofluorescence examination

After removing paraffin in xylene, the rat heart samples underwent a rehydration process using a decreasing series of ethanol solutions up to water. Subsequently, the samples were prepared for either histological examination or immunofluorescence experiments. Transversal sections of the heart were stained with haematoxylin and eosin (H&E) while others underwent the Mallory's Trichrome (Bio-Optica S.p.A., Italy) protocol to assess fibrosis. Following staining, the slides were dehydrated in an increasing ethanol series, cleared with xylene, and coverslipped using Permount. These stained ventricle sections were then analysed using light microscopy (Olympus, Japan) at magnifications ranging from 4× to 20×, with images captured digitally using a digital RGB camera (Olympus DP 20, Japan).

For IF analyses, samples were deparaffinized, rehydrated, permeabilized with 0.15 % Triton X-100, and blocked with 6 % BSA and 3 % NGS. Tissue slices were incubated overnight at 4 °C with primary antibodies: anti-TnC (Santa Cruz, Germany), anti-Cx43 (Sigma-Aldrich, Italy), and anti-c-KIT (Proteintech, UK). The samples were then incubated with secondary antibodies conjugated to Alexa Fluor 488 and Alexa Fluor 647 (Invitrogen, Italy) for 2 h at RT, followed by DAPI nuclear staining (Sigma-Aldrich, Italy). Samples were stored at 4 °C and imaged using a Zeiss LSM510 confocal microscope. Fluorescent signals for TnC and Cx43 were quantified using ZEN 3.4 software (Carl Zeiss, Germany) and normalized against DAPI. .c-Kit positive (c-Kit+) cells were assessed at 63× magnification.

2.11. Statistical analysis

When the residuals of the data did not show substantial deviations from normality (determined by the Shapiro–Wilk test) or heteroscedasticity (confirmed by Levene's test), statistical analysis was performed using two-independent samples Student's *t*-test or one/two-way parametric ANOVA, followed by Tukey's HSD post-hoc tests. These tests were employed to evaluate the significance of the effect, indicating the difference between group means. Conversely, if these assumptions were not met, non-parametric alternatives such as the Mann–Whitney *U* test or Kruskal–Wallis H test, followed by Dunn's post-hoc test, were preferred for group comparisons. $p < 0.05$ was considered statistically significant. Data were presented either as mean ± SEM in bar charts or as median and inter-quartile range (IQR) in box plots, as indicated in the caption of each respective figure.

3. Results

3.1. Chemical imaging analysis of PGF components

After defining the best production method to obtain an integrated conductive-bioartificial patch, a physico-chemical analysis was performed to evaluate the interaction between conductive peptide and PG matrix, as well as component distribution and chemical structure. A preliminary study by FT-IR Chemical Imaging was carried out using pure Fmoc-FF solution dried on the microstructured polydimethylsiloxane (PDMS) mold. The peptide follows the geometry of the mold forming a thin layer adherent to the microstructured surface, as observed in the chemical map (Fig. 1A). The characteristic peaks of the Fmoc-FF peptide are at 1690, 1633 and 1560 cm^{-1}, as reported in the literature [39] (Fig. 1B). No change to the secondary structure of the peptide was observed on the PDMS mold, showing typical peaks at 1690 cm^{-1} (β-sheet) and 1640 cm^{-1} (random coil) (Fig. 1C). Microstructured membranes PG 70/30 *w*/w with the addition of Fmoc-FF peptide (m-PGF) were prepared and assembled in a composite structure containing an inner layer of Fmoc-FF hydrogel (PGF). In Fig. 1D and E chemical map and corresponding PCA of the external surface of m-PGF are reported; corresponding spectra highlighted the presence of the characteristic bands of PLGA (ester groups at 1750 cm^{-1}) and gelatin (amide I

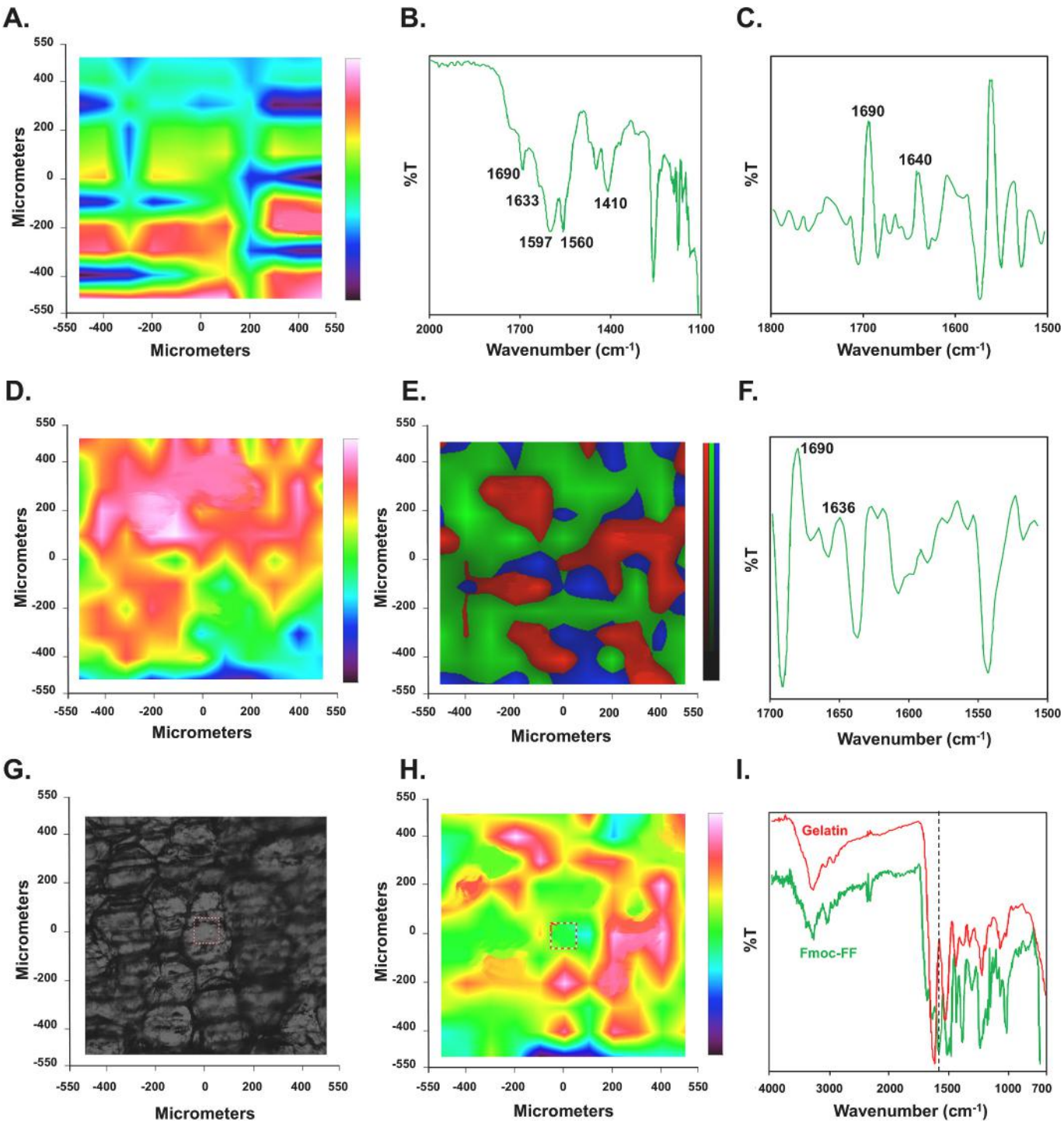

Fig. 1. FT-IR Chemical Imaging analysis of PLGA/gel/Fmoc-FF (PGF) components. A. Chemical map of pure Fmoc-FF on microstructured mold. Absorbance range intensity indicated on the bar (right): from light pink (high) to dark purple (low). B. The most representative spectrum was obtained from the chemical map in A. Characteristic peaks are indicated. C. Second derivative of the spectrum in B in the region 1800–1500 cm^{-1} to highlight the amide I deconvolution range. D. Chemical map of the monolayer PLGA/gel/Fmoc-FF (m-PGF). Absorbance range intensity indicated on the bar (right): from light pink (high) to dark purple (low). E. Principal Component Analysis (PCA) of the chemical map in D. Score scale indicated on the right: red = score 1, green = score 2, blue = score 3. F. Second derivative of spectrum acquired in a red area. G. Optical image of the inner Fmoc-FF layer. H. Chemical map at the interface between the Fmoc-FF hydrogel and bioartificial layer. Absorbance range intensity indicated on the bar (right): from light pink (high) to dark purple (low). I. Comparison between gelatin (red) and Fmoc-FF (green) spectra. The black dashed line indicates the characteristic peak of the peptide (1690 cm^{-1}). (For interpretation of the references to colour in this figure legend, the reader is referred to the web version of this article.)

at 1650 cm^{-1} and amide II at 1542 cm^{-1}). The second derivative of the spectra pointed out the presence of the bands at 1690 cm^{-1} and 1606 cm^{-1} associated with β-turn structure and of the band at 1636 cm^{-1} due to random coil conformation. This is indicative of the maintenance of the secondary structure of both conductive peptide and gelatin in m-PGF, even after mixing them with the synthetic polymer in organic solvents (Fig. 1F). FT-IR Chemical Imaging at the interface between the peptide hydrogel inner layer and m-PGF was performed. Optical image and chemical map (Fig. 1G, H) show the presence of the peptide component at the interface with the external membrane with good interaction between the inner layer and m-PGF as shown by the presence of both the prevalent PLGA band and protein-peptide bands in the area where the small peaks characteristic of the peptide, among those typical of gelatin, are observed (Fig. 1I).

3.2. Impedance spectroscopy studies

Conductivity measurements of our samples were performed using an impedance spectrometer, which evaluated the frequency-dependent capacitance through the patch's section. The setup of the measurement cell is reported on the left of Fig. 2A, while the design of a sealed cell conceived to allow measurements on the hydrated patch is shown on the right of the same figure. Initially, the electrical conductivity of the bare internal layer of the patch was evaluated. Three different oligomers, Fmoc-FF and its mixture with Fmoc-GlcS or Fmoc-GlcP in the form of supramolecular hydrogels obtained using the pH switch method were analysed (Fig. 2B) compared to pure water. No significant difference in terms of conductivity was observed among the three preparations. As the Fmoc-FF peptide allowed the formation of a more stable hydrogel, it was chosen for patch production. Fmoc-FF hydrogel was more conductive than bidistilled water (the same used for hydrogel preparation),

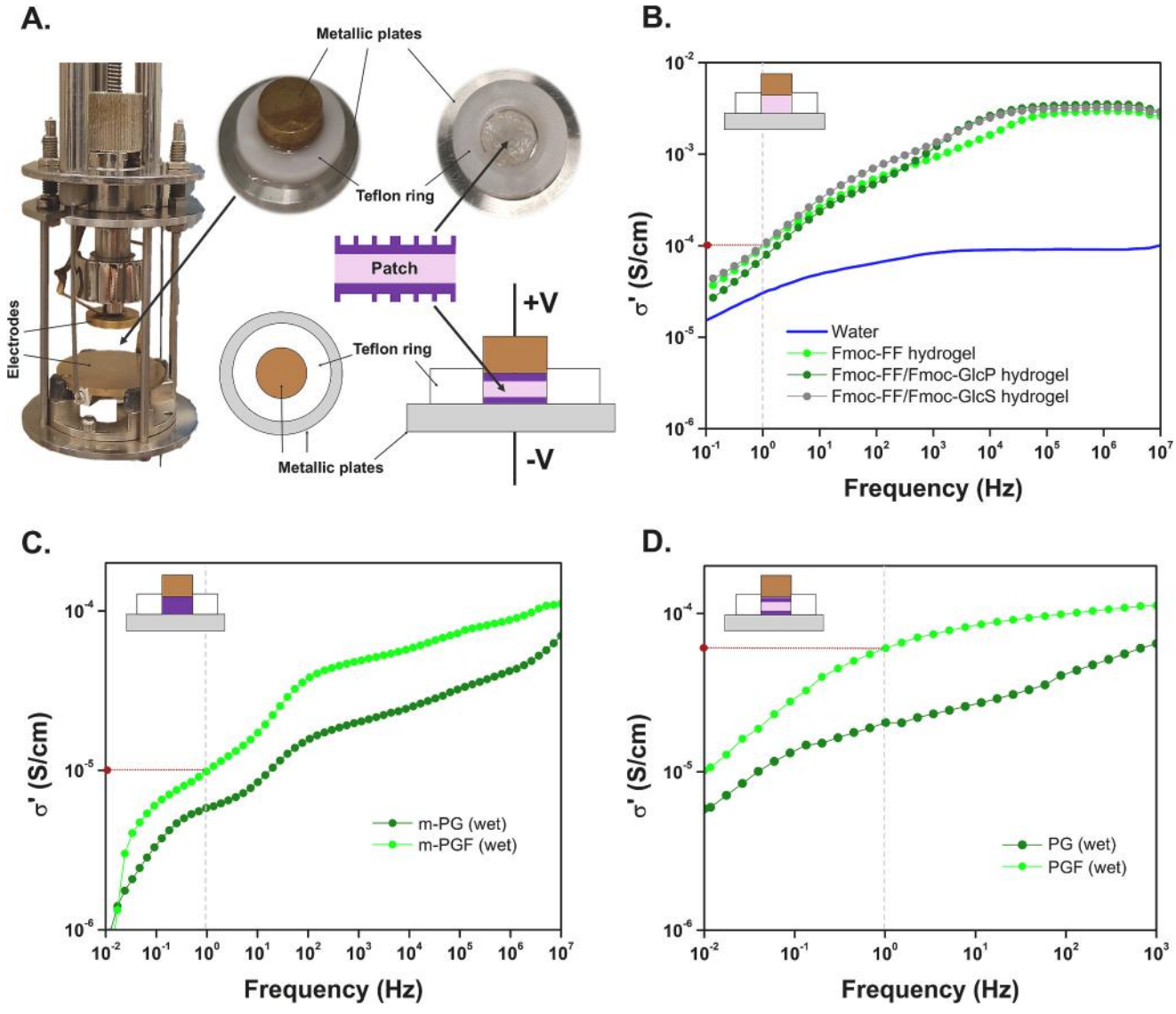

Fig. 2. Impedance spectroscopy of PLGA/gel/Fmoc-FF (PGF) components. A. Sketch of the impedance spectrometer cell (left) and of the sealed sample enclosure used for patch characterization (metallic plates and teflon ring). B. Conductive properties of three different peptides (Fmoc-FF and its co-assembled mixtures Fmoc-FF/Fmoc-GlcS and Fmoc-FF/Fmoc-GlcP) hydrogels, and bidistilled water. C. Conductivity of monolayer PLGA/gel (m-PG) and monolayer PLGA/gel/Fmoc-FF (m-PGF) in wet conditions. D. Conductivity of PLGA/gel (PG) and PGF in wet conditions. On the top left of panels B to D are reported the sketch of the sealed cell configuration used (sketch in B = only hydrogel, in C = only external microstructured layer, in D = entire assembled patch: the hydrogel between the two external microstructured layers). Grey dashed lines are traced at a stress frequency = 1 Hz (typical of myocardial tissue in physiological conditions). Burgundy dashed lines are traced to highlight the intersection with the ordinate axis of each Fmoc-FF-containing sample. (For interpretation of the references to colour in this figure legend, the reader is referred to the web version of this article.)

confirming that the peptide structure has an intrinsic conductive capability. The conductivity of the single outer microstructured layers of the patch was subsequently measured. m-PGF in wet conditions has higher conductivity compared to m-PG, confirming the reduction of the impedance of the bioartificial layer after Fmoc-FF addition (Fig. 2C). Finally, the assembled patches with (PGF) and without Fmoc-FF (PG) were analysed in wet conditions showing as PGF has higher conductivity compared to PG (Fig. 2D). PGF presents a conductivity of $6{\cdot}10^{-5}$ S cm^{-1} at 1 Hz in bidistilled water at room temperature, showing a reduction of the impedance of the PLGA scaffold, with values in line with those of myocardial native tissue [45].

3.3. Characterization of PGF

A schematic representation of PGF structure is shown in Fig. 3A. PGF was characterized *in vitro* from a morphological, mechanical and degradative point of view. SEM images show the presence of a regular micropatterning of the surface of both m-PG (Fig. 3B) and m-PGF (Fig. 3C), However, more distinct profiles were observed at a higher magnification specifically on the surface of m-PGF Fig. 3D). SEM image of the section of PGF shows the micropatterning at the level of the external surfaces and the internal fibrous layer of the patch consisting in a Fmoc-FF network having a fibrillar conformation (Fig. 3E). The image

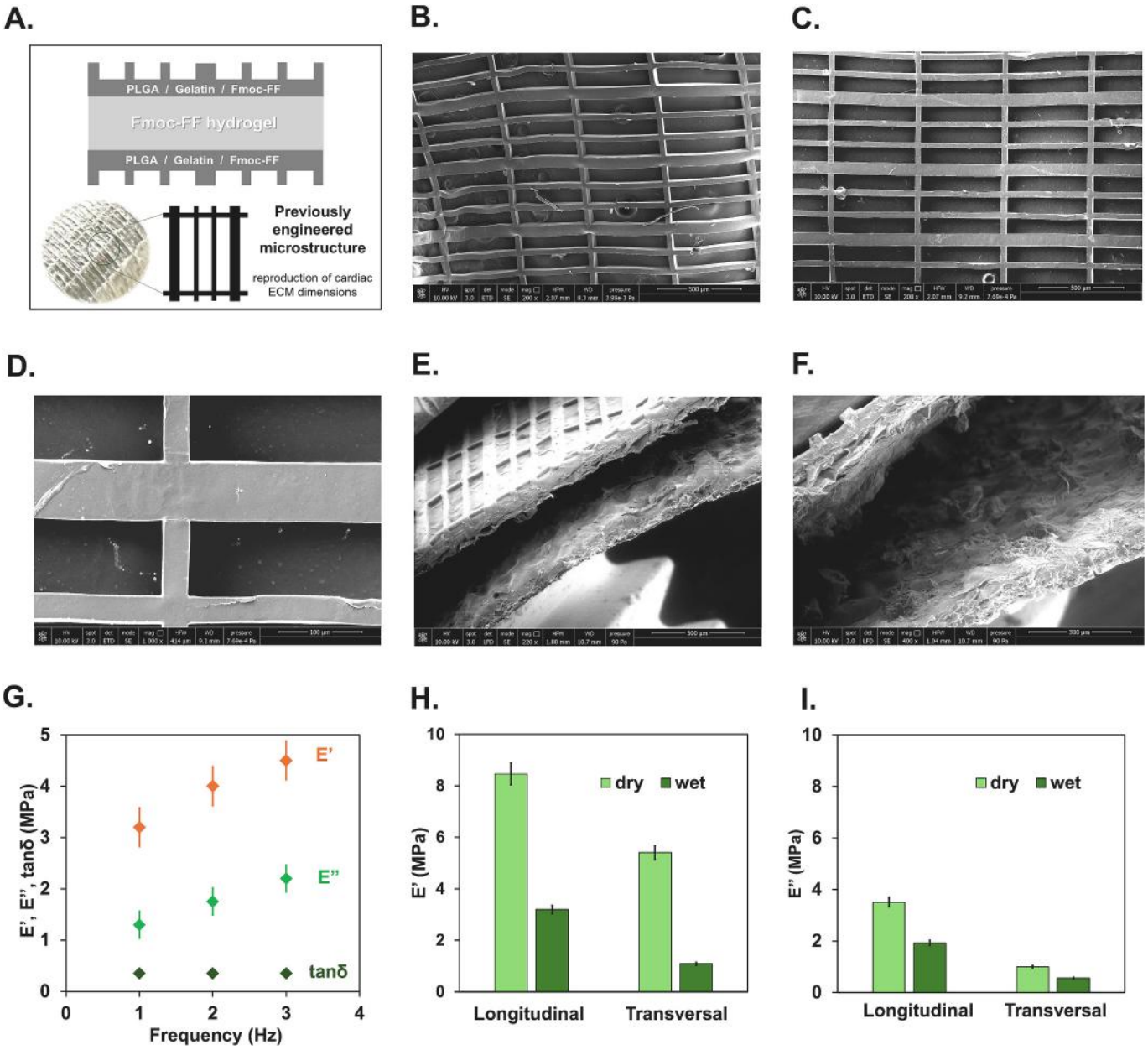

Fig. 3. Morphological and mechanical characterization of PLGA/gel/Fmoc-FF (PGF). A. Top: schematic representation of PGF structure: a Fmoc-FF hydrogel layer between two outer monolayer PLGA/gel/Fmoc-FF layers (m-PGF). Bottom: representation of the patented microstructure that reproduces the cardiac ECM dimensions. B. SEM image (mag. 200×) of the microstructured surface of PLGA/gel (PG) (absence of Fmoc-FF). Scale bar: 500 μm. *C. SEM* image (mag. 200×) of the microstructured surface of PGF (presence of Fmoc-FF). Scale bar: 500 μm. D. SEM image of a magnification (1000×) of the microstructured surface to highlight the sharp edges and show how the presence of Fmoc-FF in the blend led to a more stable structure. Scale bar: 100 μm. E. SEM image of a section of PGF (mag. 220×). Scale bar: 500 μm. F. SEM image with a magnification (400×) of the section of PGF to highlight the fibrous inner layer of Fmoc-FF hydrogel. Scale bar: 100 μm. G. DMA analysis of PGF: storage modulus (E′), loss modulus (E″) and damping factor (tanδ) at 3 different frequencies. Mean ± SEM ($n = 3$). H. Storage modulus (E′) of PGF tested along two directions (longitudinal and transversal) in dry and wet conditions. Mean ± SEM (n = 3). I. Loss modulus (E″) of PGF was tested along two directions (longitudinal and transversal) in dry and wet conditions. Mean ± SEM (n = 3).

at higher magnification consents to point out the fibrous inner layer (Fig. 3F) which derives from the macro-architecture of Fmoc-FF cylinders formed by anti-parallel β-sheets interconnected by the π-stacking interactions between fluorenyl groups and phenyl rings [34,35].

Dynamical Mechanical analysis (DMA) was carried out on PGF and PG in dry and wet conditions at 1 Hz and 37 °C. The storage modulus, E′, measured for PG along the longitudinal direction, was 13.0 ± 0.8 MPa and 6.0 ± 0.2 MPa, in dry and wet conditions, respectively. E′ for PGF measured along the longitudinal direction was 8.5 ± 0.3 MPa and 3.3 ± 0.3 MPa, in dry and wet conditions, respectively. Fmoc-FF has thus determined a decrease in the stiffness of the scaffold, making it more flexible and compatible with the characteristics of the cardiac tissue [46].

Mechanical properties (E′, E″, tanδ) of PGF were measured at frequency sweep of 1, 2 and 3 Hz and were found to linearly increase with the stress frequency (Fig. 3G), regardless of stretching direction and dry or wet conditions, in line with a study carried out on animal tissue samples [47]. The results reported in Fig. 3H-I and refer to a stress frequency of 1 Hz, typical of a healthy myocardial tissue in physiological conditions (Fig. 3H-I). A considerable difference in the mechanical properties in response to the longitudinal and transverse stretching of PGF with respect to the microstructure was observed, highlighting anisotropy similar to that found in the natural myocardium. Storage modulus (E′) was much greater than the Loss modulus (E″), indicating a predominance of the elastic behaviour over the viscous one, both in dry and wet conditions.

Moreover, degradation tests were conducted on PG and PGF samples (Fig. 4 A-E). A morphological analysis was carried out at different degradation times; some representative images are reported to compare the effect of the incubation medium on patch stability. SEM analysis of the PG surface after 7 days of incubation shows the presence of small porosities and some larger pores while the rectangular profiles are still present and rather well preserved (Fig. 4A). On the contrary, SEM analysis of the PGF surface at longer times of incubation (after 14 days) shows the presence of only small porosities at the level of surface structure and the maintenance of micropatterning reliefs (Fig. 4B). The image of PG section after 7 days of incubation shows the presence of well-distributed micro-porosities at the level of the whole section of the external layer (Fig. 4C). The image of PGF section at 14 days of degradation points out the presence of small pores close to surfaces while the deeper part of the section shows a dense structure (Fig. 4D).

A higher degradation stability of the polymeric structure in the presence of Fmoc-FF peptide was confirmed by GPC analysis. The trends of average molecular weight (Mw) variation with degradation time for m-PG and m-PGF are reported (Fig. 4E). GPC analysis of m-PG and m-PGF shows a reduction of average molecular weight (Mw), which can be explained by the fact that polymeric matrices absorb water over time and consequently the PLGA polymer chains in the bulk samples break up, causing a molar mass reduction. The reduction of Mw in the first hours can be associated with the effect of enzymatic hydrolysis of MMP-9, acting on PLGA ester groups and mainly on gelatin and the peptide. At the same time, the PBS solution caused a gradual reduction in molecular weight over 4 weeks due to its hydrolytic effect. A more pronounced splitting of the polymer chains in the m-PG compared to the m-PGF was observed for up to 4 weeks. These results are in line with those obtained using morphological analysis.

The analysis of pH in the degradation medium for PGF showed the maintenance of pH at a physiological level over time (Fig. 4F). This means that, although the sample starts to degrade in a short time, the degradation products do not alter the pH of the medium, as previously observed for the same analysis performed on PG [16]. Moreover, this result also indicates that the Fmoc-FF hydrogel prepared by the pH switch method does not alter the pH of the surrounding medium throughout the entire incubation period. This is a positive effect in view of the *in vivo* biocompatibility of the PGF, thereby avoiding inflammatory effects.

3.4. In vitro biological comparison between m-PG and m-PGF

Biocompatibility investigation was conducted by flow cytometry, assessing the cell viability of two relevant cell types: H9C2 and hMSCs. The m-PG and m-PGF were incubated with both cell types for 24, 48, and 72 h. No cytotoxic effects were observed in cell viability assays compared to the control, demonstrating excellent cytocompatibility of both patches and complete harmlessness of the electroconductive component (Fig. 5A).

Next, we aimed to verify whether Fmoc-FF addition could foster patch effects on cell elongation and alignment. Fluorescent microscopy was employed to evaluate changes in the cellular morphology of H9C2 cells cultured on both m-PG and m-PGF for 3, 5, and 7 days (Fig. 5B). Starting from day 3, the cells grown on m-PGF appeared to be more aligned in parallel with each other compared to those grown on m-PG (Fig. 5B). Additionally, the cells grown on m-PGF for 3 and 7 days had a significantly more elongated morphology than those grown on m-PG (44.05 ± 2.26 μm *vs* 31.3 ± 1.36 μm at 3 days and 51.84 ± 2.5 μm *vs.* 40.31 ± 1.46 μm at 7 days, $p < 0.001$), as shown in Fig. 5C. Additionally, H9C2 cells cultured on m-PGF exhibited a well-organized actin cytoskeleton, with actin fibers predominantly oriented along the major cellular axis, consistent with the observed elongated morphology (Fig. S3). The comparison highlighted that the electroconductive component induced a better organized cell-cell arrangement, displaying a more elongated phenotype, which could indicate an early stage of cellular differentiation.

We then evaluated by qRT-PCR whether culturing hMSCs on m-PG and m-PGF for 14 days could influence gene expression related to cell differentiation. The evaluated genes included KIT, a tyrosine kinase receptor that plays a pivotal role in stem cell self-renewal [48], GATA4, a zinc finger transcription factor, crucial in cardiac development and implicated in directing hMSCs toward a cardiac lineage [49], MEF2C, a member of the myocyte enhancer factor-2 family and essential for myogenesis and muscle differentiation [50], and NKX2.5, a homeobox-containing transcription factor acting as a regulator of cardiac morphogenesis [51]. We observed that hMSCs seeded on either m-PG or m-PGF for 14 days showed significant downregulation of KIT and upregulation of GATA4 compared to the control cells seeded in 2D (Fig. 5D). In addition, the cells cultured on m-PGF displayed significant downregulation of KIT and a slight yet not-significant upregulation of GATA4, MEF2C and NKX2.5 compared to those cultured on m-PG (Fig. 5D). Cell differentiation thus appeared to be partially augmented by the electroconductive component.

A longitudinal study of hiPSC-CM behaviour on both patches revealed that these cells consistently maintained their synchronous beating activity only on m-PGF for the entire 30-day duration, emphasising the dynamic interaction of cells with this patch (Video S1). Further, the addition of Fmoc-FF confirmed the ability to maintain the integrity of patch microtopography throughout the entire 30-day period (Fig. 5E), a crucial feature that may sustain its effectiveness for repairing infarcted cardiac tissue [52].

Based on the positive effects exerted on cell elongation, alignment and differentiation, as well as prolonged maintenance of microtopography, the bilayer version (PGF) was selected for further analyses.

3.5. In vitro biological study of PGF

Biocompatibility of bilayer PGF was investigated by flow cytometry, employing both H9C2 cardiomyoblasts and hMSCs at 24, 48, and 72 h. Results demonstrated no cytotoxic effects compared to the control cells (Fig. 6A), again highlighting the optimal biocompatibility of the patch.

Next, we assessed whether PGF could affect cardiac cell beating. To this purpose, hiPSC-CMs were cultured for 24 h on PGF, loaded with the calcium indicator Fura-2AM, and observed in real-time using fluorescence microscopy to quantitatively characterise spontaneous changes in intracellular calcium levels ($[Ca^{2+}]_i$). Data were collected over 15 min to

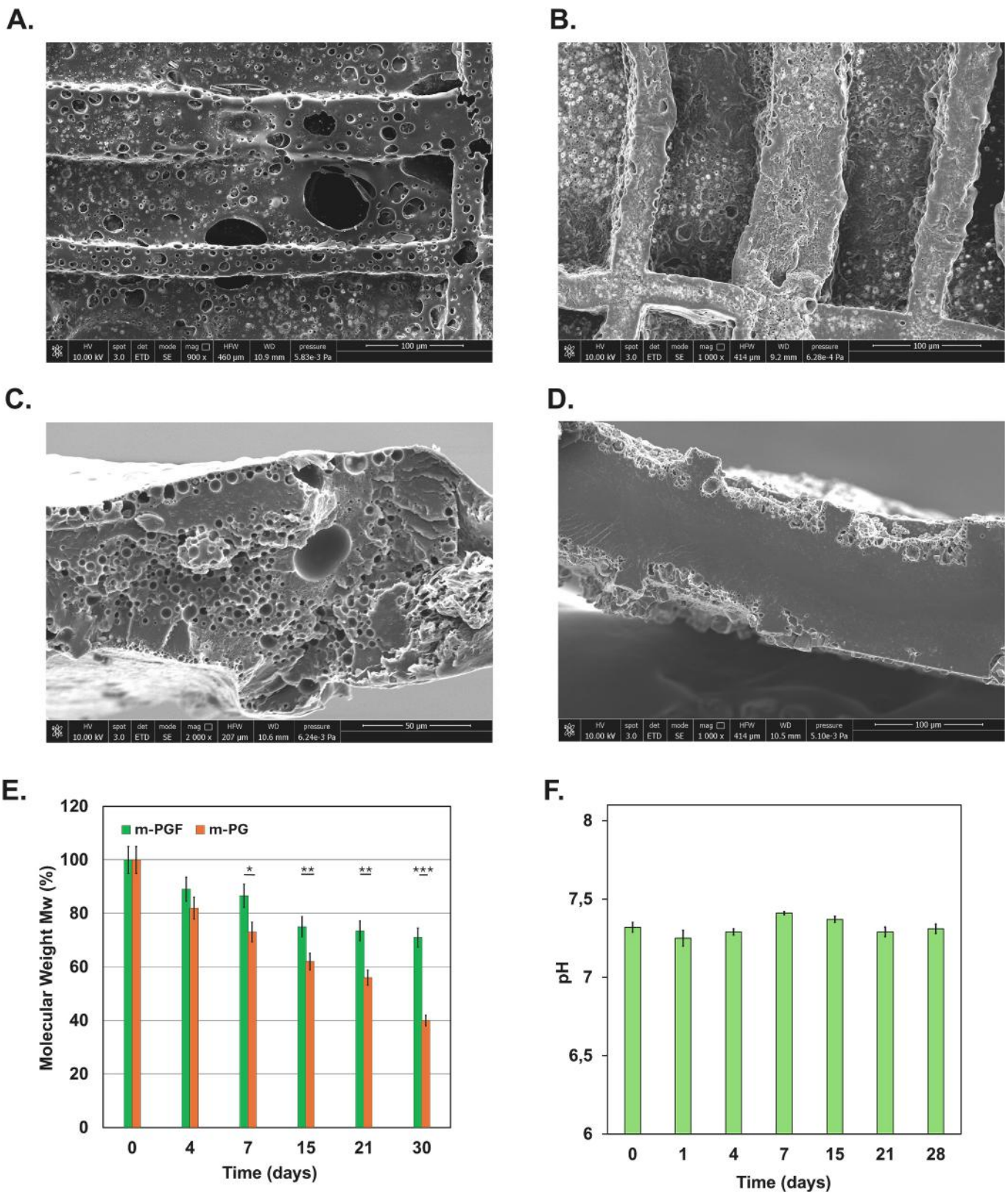

Fig. 4. Degradation study of PLGA/gel (PG) and PLGA/gel/Fmoc-FF (PGF). A. SEM image of a magnification (900×) of the surface microstructure of PG after 7 days of incubation in an oscillated bath at 37 °C in PBS and MMP-9. Scale bar: 100 μm. B. SEM image of a magnification (1000×) of the surface microstructure of PGF after 14 days of incubation. Scale bar: 100 μm. *C. SEM* image of a magnification (2000×) of the section of PG after 7 days of incubation. Scale bar: 50 μm. D. SEM image of a magnification (1000×) of the section of PGF after 14 days of incubation. Scale bar: 100 μm. E. Trend of Molecular weight (Mw) percentage *versus* degradation time for monolayer PLGA/gel (m-PG) and monolayer PLGA/gel/Fmoc-FF (m-PGF). Statistical analysis by two-way t-Test (*$p < 0.05$, **$p < 0.01$, ***$p < 0.001$). Mean ± SEM (n = 3). F. pH values of the supernatant of PGF at different degradation times. Mean ± SEM (n = 3).

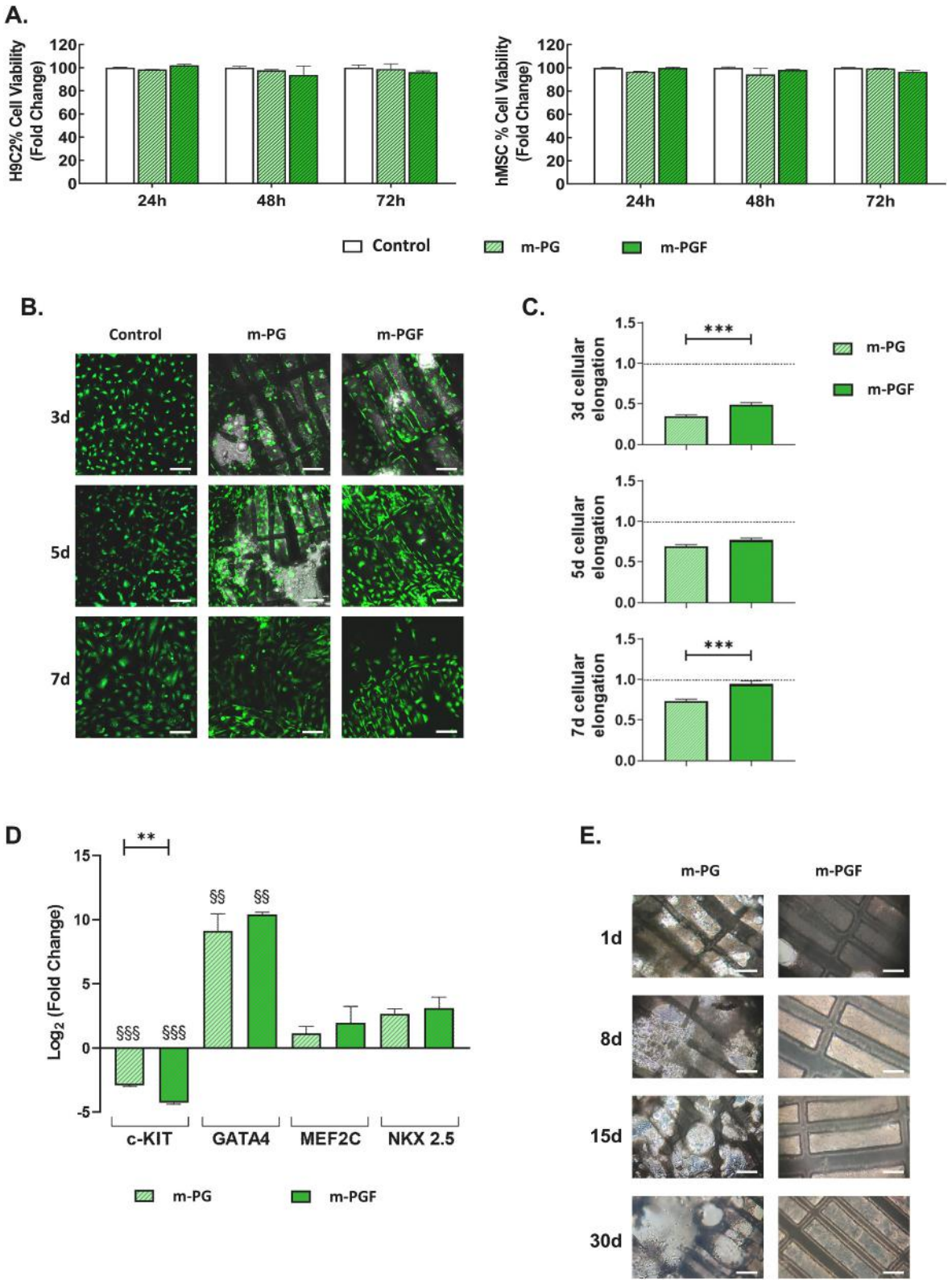

Fig. 5. Impact of monolayer PLGA/gel (m-PG) and monolayer PLGA/gel/Fmoc-FF (m-PGF) on cell cultures. A. Viability of H9C2 cells and hMSCs after seeding on m-PG and m-PGF (mean ± SEM, $n = 3$) compared to 2D control cells. B. Representative fluorescent images of Calcein-AM live stained H9C2 cells cultured in 2D, on m-PG or m-PGF. Scale Bar: 100 μm. C. Fold-change of H9C2 elongation (mean ± SEM, n = 3). Data are normalized to the 2D control (dashed line). D. Gene expression in hMSCs grown on m-PG or m-PGF for 14 days. Data are normalized to the 2D control. Data are expressed as $\log_2$ fold change ($2^{-\Delta\Delta Cq}$) ± SEM (n = 3). E. Phase-contrast images of hiPSC-CMs seeded on m-PG or m-PGF from 1 to 30 days. Scale Bar: 50 μm. ***$p < 0.001$, **$p < 0.01$ m-PG *vs* m-PGF. §§§ $p < 0.001$, §§ $p < 0.01$ m-PG and m-PGF *vs* 2D control.

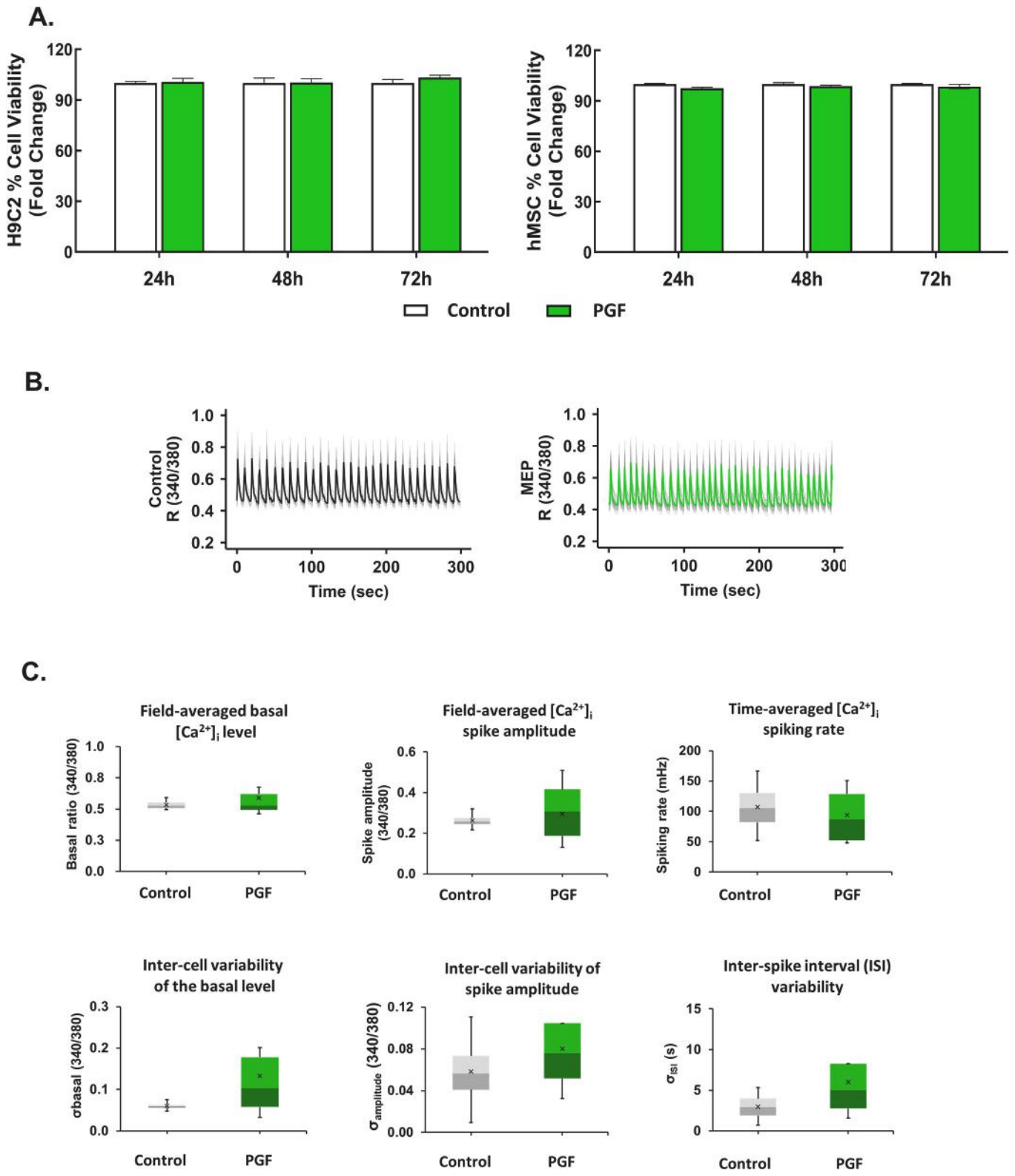

Fig. 6. *In vitro* evaluation of bilayer PLGA/gel/Fmoc-FF (PGF). A. Viability of H9C2 cells and hMSCs after seeding on PGF (mean ± SEM, $n = 3$) compared to 2D control cells. B. Superimposition of the $[Ca^{2+}]_i$ time courses recorded from all the cells within the same optical field (n = 3), namely spontaneous beating of hiPSC-CMs cultured for 24 h in 2D control or on PGF. C. Quantitative analyses of $[Ca^{2+}]_i$ dynamics. For each experimental condition, field-averaged basal $[Ca^{2+}]_i$ level, field-averaged $[Ca^{2+}]_i$ spike amplitude, and time-averaged $[Ca^{2+}]_i$ spiking rate are shown in the upper panel, from left to right, respectively. In the lower panel, a measure of variability for each one of the above parameters is shown (*i.e.*, between-cell variability for basal levels and spike amplitude, and inter-spike interval (ISI) variability as a measure of spiking rate regularity). All boxplots represent the median and IQR.

estimate mean basal calcium levels and the mean spike amplitude, along with their respective between-cell variability. Additionally, measures of beating frequency and regularity were obtained by evaluating the time-averaged $[Ca^{2+}]_i$ spiking rate and inter-spike interval (ISI) variability. In this regard, no differences were observed in any of these parameters when comparing hiPSC-CMs cultured on PGF with those cultured in 2D control conditions (Fig. 6B and C). The typical oscillations in cytosolic calcium and synchronised beating were observed (Fig. 6B). This finding suggests that the cells exhibited proper cytosolic connectivity due to the presence of gap junctions. Specifically, a contraction and relaxation performance with a frequency of approximately 0.1 Hz was registered in all experiments (Fig. 6C, upper right panel).

Altogether, these findings indicate that incorporation of electroconductive material in bilayer patches does not perturb the physiological intracellular and intercellular calcium handling of hiPSC-CMs.

3.6. *In vivo implantation of PGF in a murine model of ischaemia/reperfusion (I/R)*

PGF was epicardially implanted in rat hearts subjected to I/R and *in vivo* therapeutic effectiveness was evaluated after 4 weeks through histological and immunofluorescence analyses.

In the I/R group, H&E staining showed tissue damage with a scarred area and thinning of the ventricular wall. The damaged area contained clusters of viable cardiomyocytes surrounded by areas of interstitial fibrosis (Fig. 7A, red asterisks). Upon magnification, an abundant cell infiltrate (Fig. 7A, red square), including macrophages with hemosiderin (Fig. 7A, red arrows), could be observed between the deposited collagen. The simultaneous presence of consolidated fibrosis in some parts of the infarcted area and granulation tissue in others suggests that the healing process is still evolving 4 weeks after the I/R event. Conversely, in the I/R + PGF group, the myocardial morphology was primarily preserved, and a regular pattern of fibre arrangement was maintained except for mild sporadic tissue lesions (Fig. 7A). Upon higher magnification and compared to the I/R group, the cardiac tissue under the patch appeared more similar to the healthy myocardium in the remote zone, with fewer collagen deposits intercalated between viable cardiomyocytes and very limited cell infiltrates (Fig. 7A, red square). In addition, functional vessels were visible at the interface between the myocardium and PGF patch (Fig. S4).

These findings underscore a stark contrast in the preservation of myocardial architecture between the experimental group receiving PGF and the I/R group, highlighting the profound impact of the treatment.

Immunofluorescence staining of the sarcomeric protein TnC and the gap junction component Cx43 was used to evaluate tissue integrity, myocardial cell survival, and cell-cell connectivity essential for electrical coupling. In the I/R group, low levels of TnC and Cx43 indicated significant left ventricle damage, pointing out the loss of proper tissue morphology and cell-to-cell connection between neighbouring cardiomyocytes, particularly highlighted by Cx43 lateralization (Fig. 7B, red arrows). In contrast, the I/R + PGF group showed increased expression of TnC and Cx43, along with the recovery of a correct Cx43 localization at intercalated discs (Fig. 7B). Quantitative analysis revealed a significant recovery of TnC from 32.5 ± 10.2 % in the I/R group to 74.6 ± 11.6 % in the I/R + PGF group ($p < 0.05$), and Cx43 from 2.8 ± 1.2 % to 65.7 ± 25.6 % ($p < 0.05$) (Fig. 7C). We also investigated whether PGF could recruit undifferentiated c-Kit+ cell precursors *in vivo*. Confocal immunofluorescence analysis highlighted a > 2.5-fold increase in c-Kit+ cells located at the epicardial level in the I/R + PGF group compared to the I/R group (Fig. 7D and E). Altogether, these results suggest an increase in viable myocardial cells, an improvement in electrical coupling, and an enhancement in c-Kit+ cell recruitment following PGF treatment.

To evaluate the effect of PGF on myocardial fibrosis at 4 weeks after implantation, the collagen scar tissue was observed using both Mallory's staining analysis and FT-IR Chemical Imaging of infarcted hearts. The blue colour of collagen deposition was evident in the section area of infarcted hearts (Fig. 8A). Chemical Imaging analysis performed on the same areas showed an altered protein profile (Fig. 8B), allowing the observation of an evident increase of bands corresponding to collagen deposition (dark areas) (Fig. 8C). The I/R + PGF group showed a decreased extension collagen scar as evidenced by Mallory's staining (Fig. 8D), indicating lower fibrosis in the patch-treated rat hearts. Accordingly, FT-IR Chemical Imaging analysis, performed on I/R + PGF myocardial tissue sections, showed a protein profile having bands attributable to a secondary structure of more normal tissue (red areas) (Fig. 8E-F). Overall, these two complementary analyses suggest that PGF can reduce cardiac fibrosis.

4. Discussion

With advances in TE and materials science, bioartificial, biomimetic, biodegradable and mechanically compliant 3D patches that allow optimal tissue integration, complete reabsorption, and simultaneous tissue restoration are expected to be the next-generation devices for the treatment of MI. Here, we report a newly implemented acellular, biodegradable and biomimetic epicardial patch providing synergic physico-chemical, mechanical and electrical cues. The patch is endowed with a proprietary microstructure that induces endogenous cell growth and alignment, and it incorporates a degradable electroconductive component for ameliorating tissue integration with a dynamic epicardium surface. Notably, this patch shows suitable mechanical properties in agreement with those of native cardiac tissue, improved conductivity, optimal biocompatibility, easy apposition and suturability, favourable tissue preservation ability, precursor cell enrichment, and a simultaneous reduction of fibrosis at the level of the infarcted area in the complete absence of any arrhythmic events.

Interest in the use of electroconductive polymers has significantly grown over the years [22,53]. In light of their potentialities and the rising interest in the field, many electroconductive materials/patches have been recently reported for cardiac TE [18]. This arises from the need to allow a patch in contact with the cardiac tissue not to impede the propagation of electrical signals [48]. These encompass stretchable bioelectronic interfaces for electrocardiogram signal recording and electrical pacing [27], injectable cardiac patch hydrogels with shape memory properties for use in atrial fibrillation [26] or MI [25] treatment, as well as diagnostic/therapeutic integrated platforms providing a promising monitorable treatment protocol for cardiac disease [31].

However, many electrically conductive polymers or nanocomposites may present disadvantages in terms of toxicity, lack of degradability and re-absorbability *in vivo*. To overcome these limitations, the use of self-assembling peptide nanostructures with enhanced semi-conducting characteristics has emerged as a possible strategy for applications in healthcare research [54,55]. Moreover, the employment of Fmoc-FF in biomedical device functionalization is widely recognized for its unique mechanical and biophysical properties [55]. Our preliminary studies performed on three different self-assembling peptides, two of which containing glucosamine moieties, favored the use of the Fmoc-FF peptide. Although no substantial differences in conductivity were observed among the three different kinds, the hydrogel formed by the pristine Fmoc-FF peptide exhibited better consistency. Importantly, the level of electrical conductivity of the Fmoc-FF hydrogel, obtained by the pH switch method, showed the same order of magnitude electrical signal transduction level in native heart tissue ($\approx 10^{-4}$ S cm^{-1}). We therefore started by evaluating the feasibility of appropriately implementing our patch with Fmoc-FF into all the constituent layers of our patch, including the internal layer containing Fmoc-FF in hydrogel form and the microstructured bioartificial external layers. The first important aspect was to verify that the method used to incorporate the conductive component into the patch structure did not negatively affect the fundamental structural and functional properties of the patch itself, nor those of the selected conductive peptide. A key aspect of this

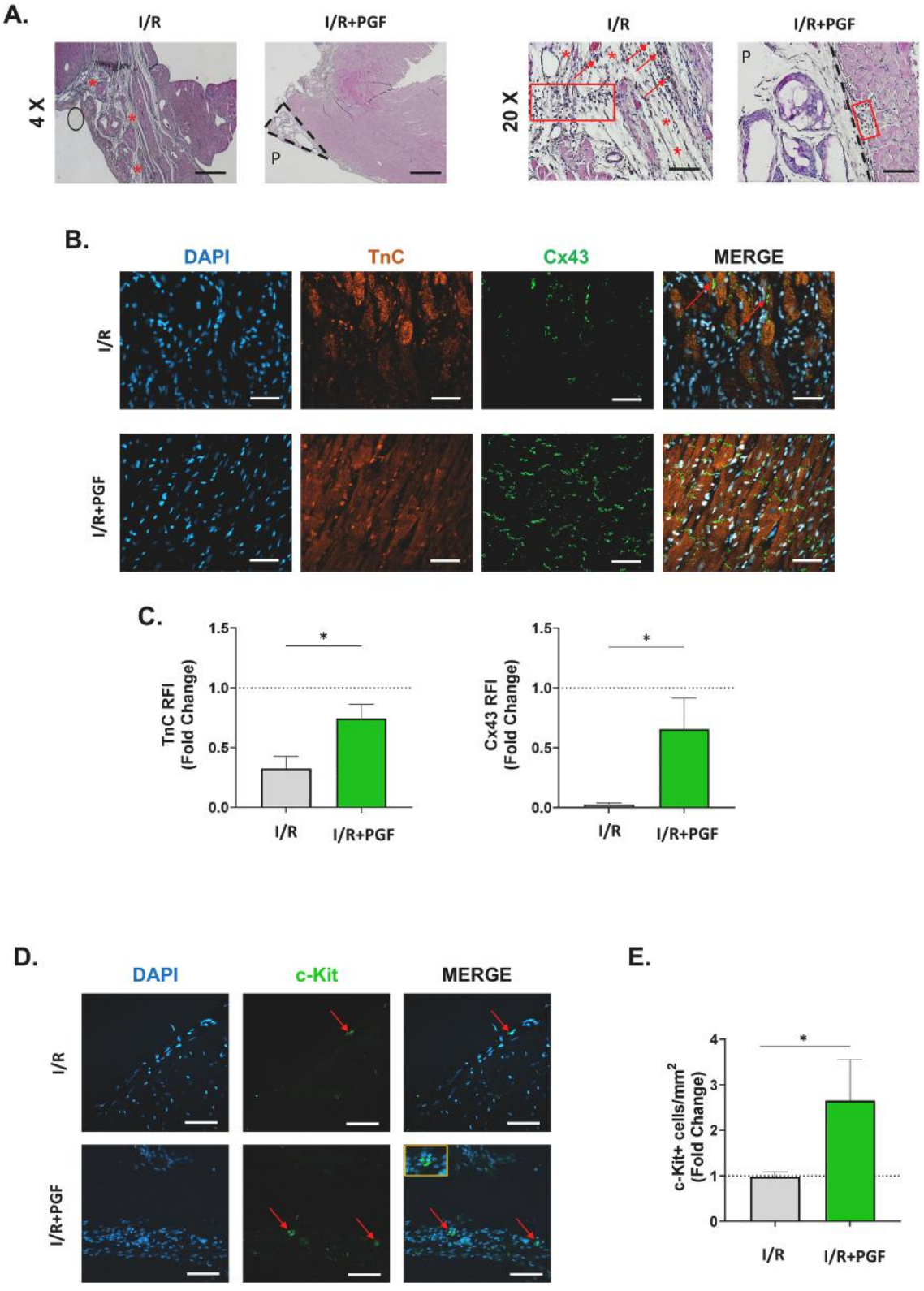

Fig. 7. *In vivo* evaluation of PLGA/gel/Fmoc-FF (PGF) in a rat model of myocardial I/R. A. Representative images of the infarcted region in the left ventricle of I/R and I/R + PGF groups stained with HE at lower (4×) and higher (20×) magnification. Scale Bar 4×: 200 μm, Scale Bar 20×: 50 μm. Red asterisks indicate interstitial fibrosis, red squares indicate cell infiltrates and red arrows indicate macrophages with hemosiderin. Dashed lines delimit the patch (P) area. B. Representative confocal microscopy high-magnification image of the subepicardial region (under the patch for the I/R + PGF group, or in the infarcted area for the I/R group) showing nuclei (blue), TnC (orange) and Cx43 (green) immunofluorescent staining. Scale Bar: 50 μm. Red arrows indicate Cx43 lateralization. C. Graphs show fold change of fluorescent intensity (RFI) for TnC and Cx43 normalized against Sham hearts (mean ± SEM, $n = 4$). *$p < 0.05$. D. Representative confocal images showing c-Kit+ cells (red arrows) in the subepicardial region of the left ventricle (under the patch for the I/R + PGF group, or in the infarcted area for the I/R group). The insert shows c-Kit+ cell magnification. E. Graphs show fold change of c-Kit+ cells normalized against the Sham group. Scale Bar: 50 μm. c-Kit: green; DAPI: blue ($n = 3$). **$p < 0.01$, *$p < 0.05$. (For interpretation of the references to colour in this figure legend, the reader is referred to the web version of this article.)

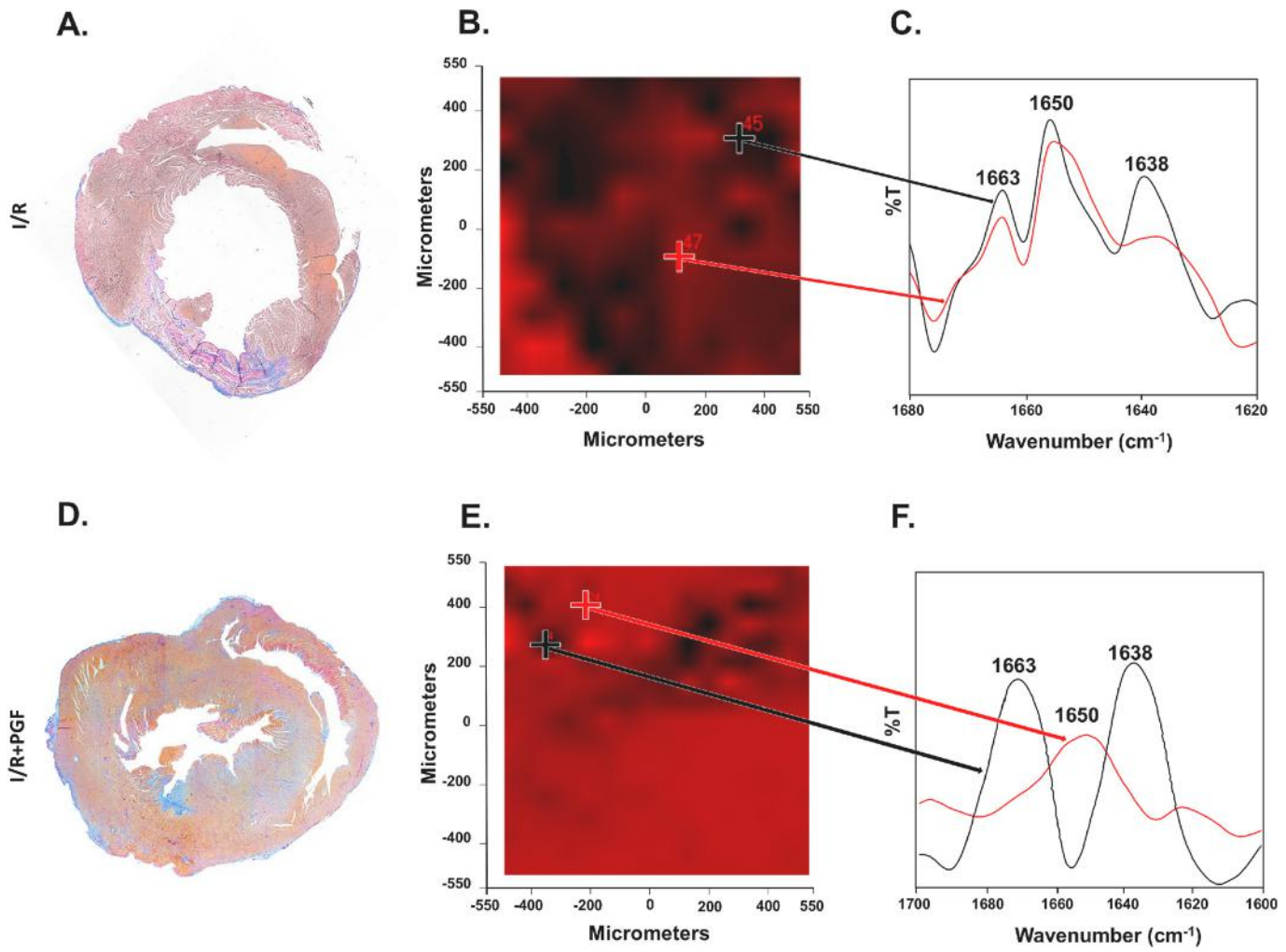

Fig. 8. *In vivo* evaluation of the impact of PLGA/gel/Fmoc-FF (PGF) on cardiac fibrosis. A. A representative Mallory's Trichome stained cross-section of the whole rat heart for I/R. B. FT-IR Chemical Imaging correlation map as a function of the band at 1663 cm-1 (taken as a reference to identify collagen deposition) to evaluate the protein conformational profile of myocardial tissue of the I/R group. Areas ranging from black to red are highlighted (black = high correlation, red = low correlation). C. Corresponding second derivative of infrared spectra for I/R tissue (black and red spectra are acquired respectively in the black and red areas of the chemical map in B - exact points indicated by the "+"). D. A representative Mallory's Trichome stained cross-section of the whole rat heart for I/R + PGF. E. FT-IR Chemical Imaging correlation map as a function of the band at 1663 cm-1 (taken as a reference to identify collagen deposition) to evaluate protein conformational profile of myocardial tissue of I/R + PGF group (after PGF implant). F. Corresponding second derivative of infrared spectra for I/R + PGF tissue (black and red spectra are acquired respectively in the black and red areas of the chemical map in E - exact points indicated by the "+"). (For interpretation of the references to colour in this figure legend, the reader is referred to the web version of this article.)

configuration is the functional position of the inner hydrogel, which serves multiple roles. It acts as a flexible, hydrated, core that ensures the adhesion between the two outer microstructured layers, maintaining the patch's integrated bilayer structure. Furthermore, by incorporating the same conductive Fmoc-FF peptide as the outer layers, the hydrogel ensures a homogenous electrical conductivity throughout the entire patch, which is critical for its function. The fibrous network of the Fmoc-FF hydrogel also contributes to the overall mechanical properties of the final construct. Additionally, its hydrated structure makes the hydrogel an ideal reservoir that could be loaded with active ingredients for controlled therapeutic delivery.

FT-IR Chemical imaging was useful to confirm the maintenance of the peptide secondary structure after blending with synthetic and biological components and, at the same time, the strict preservation of surface bioinspired micropatterning during the manufacturing phase.

In addition, as desirable, the conductivity values measured for m-PGF were found to be higher than for its m-PG counterpart. Considering that the native myocardium's conductivity can reach up to $5{\cdot}10^{-5}$ S cm^{-1} [45], the value at 1 Hz for PGF resulted in $6{\cdot}10^{-5}$ S cm^{-1}, suggesting that the electrical impedance of the patch after Fmoc-FF addition is reduced as required for this purpose. The increase in conductivity is important, and even more so if we consider that the analysis was conducted in bidistilled water and not in a buffer solution, allowing a more sensitive measurement of the intrinsic conductivity of the patches. Moreover, all measurements refer to analysis using a parallel plate capacitor through the entire section of the patch (transverse measurement, as shown in Fig. 2A) and not on the four-point-probe surface (longitudinal measurement) as in other *in vitro* studies [56,57]. The transverse conductivity value is reported to be at least one order of magnitude smaller than the longitudinal one [58].

The presence of conductive peptide into the construct makes it more flexible, as indicated by the DMA and at the same time more stable in an aqueous environment, maintaining pH values within the physiologic range. Mechanical anisotropy of PGF was in accordance with cardiac tissue, while a storage modulus reduction after incorporation of the peptide component was observed [56].

The biodegradability of a patch is a crucial feature, and the degradation rate strongly depends on biomaterial composition [59]. At the

same time, biodegradability in implanted devices cannot be overstated, and the degradation rate should match the tissue regeneration rate [60]. In the *in vitro* biological tests conducted with hiPSC-CMs, the microenvironment of the cell culture highlighted that the presence of Fmoc-FF resulted in a reduction of the biodegradability rate. This microstructural preservation of PGF promoted better hiPSC-CM distribution and persistent rhythmic cell beating after a 30-day culture. This distinctive feature of PGF can not only preserve an optimal environment for tissue regeneration but also offer prolonged mechanical support to the infarcted cardiac wall, which can become thin and less resilient after MI [14]. Indeed, a ventricular rupture is a serious and fatal complication that can potentially occur in some post-infarction scenarios. The permanence of this patch *in situ* might strengthen the cardiac wall, thus preventing its rupture during the remodelling process [61]. The slower degradation rate of the patch with extended maintenance of the microstructure can also prolong the epicardial activation, in line with the observed higher number of c-Kit+ cells 4 weeks after the implantation (see below).

The employment of non-degradable conductive materials has been shown to enhance stem cell adhesion, proliferation, and differentiation [62–65], yet little is known about the cellular effects exerted by biodegradable Fmoc-FF self-assembling peptides [42]. The typical Fmoc-FF self-assembly into aligned, instead of randomly organized, nanostructures can potentially guide stem cell alignment, thus affecting cell fate. [34]. Our results demonstrated that PGF improved cardiomyoblast adhesion and elongation, as well as stemness markers downregulation in hMSCs. We propose that while the microstructured, bioartificial component of the patch provides a biocompatible microenvironment to the cultured cells, the conductive component fosters cell morphological changes and differentiation.

In vivo validation of PGF was conducted on a small animal I/R model. Notably, none of the animals developed arrhythmias, which is critically important for clinical translation. Throughout the 4-week *in vivo* studies, no patches ruptured, demonstrating their ability to withstand the high mechanical stress conditions of the left ventricular system. Cardiac morphological staining evidenced the therapeutic effect of PGF on myocardial repair. The I/R group exhibited loss of cardiac left ventricular structure, including cardiomyocyte death, wall thickness thinning, and fibrosis formation.

Confirming the histological results, chemical imaging analysis detected a partially preserved protein profile in the tissue treated with PGF compared to the I/R group, as can be seen from the collagen conformation showing a more ordered secondary structure. This behaviour was observed for the entire section of the ventricular wall, *i.e.* from the epicardium to the endocardium. PGF possibly promoted the healing process through mechanical compensation and electrical integration, significantly relieving ventricular remodelling and maintaining wall thickness. Although several electroconductive materials used in cardiac patch production have already been shown to enhance the expression of sarcomeric (i.e.: Tn, actin) and gap junction (i.e: connexin-43) genes/proteins, however, they were not organic and biodegradable materials as Fmoc-FF is [5,66]. To the best of our knowledge, there is no literature associating Fmoc-FF with an elevated expression of typical myocardial proteins.

To better explore the eventual myocardial repair, the infarct zones in the I/R and I/R + PGF groups were analysed by immunofluorescence staining. The expression level of TnC and Cx43 in the infarcted area was much lower in the I/R group, suggesting that cardiomyocytes underwent cell death and intercellular electrical communication was greatly reduced. In addition, in both the infarcted area and border zone, Cx43 distribution was altered in viable cardiomyocytes, showing the expected MI-induced Cx43 lateralization, typical of damaged cardiac tissue. Altered gap junction distribution after MI correlates with changes in signal conductive velocity, with consequent potential pro-arrhythmic effects and contractile dysfunction [67]. Instead, PGF implantation preserved TnC and promoted the myocardial electrical coupling by not only sustaining Cx43 expression but also its proper distribution at the level of the intercalated discs. The correct Cx43 distribution is crucial for cardiac function after MI, as well-organized intercalated discs facilitate improved cell-to-cell communication and the proper action potential propagation [68]. Therefore, future investigations should focus on further elucidating PGF's capacity to promote myocardial function recovery by evaluating the myocardial contractility in post-MI rat hearts following patch application. We observed that the epicardial implantation of PGF also induced c-Kit+ cell recruitment, which may represent an important step in myocardial tissue preservation. Physiologically, c-Kit+ cells are predominantly located in the subepicardial regions and interstitial spaces, exhibiting a gradient from the epicardium to the endocardium [69–71]. The activation of epicardium in response to damage triggers a series of events, including upregulation of gene expression, proliferation, and migration of epicardial-derived cells (EPDCs). The latter process occurs through an epithelial-mesenchymal transition (EMT) and primarily results in the formation of non-cardiomyocyte lineages, which seem to play a crucial role in myocardial regeneration [69,72]. According to the recent literature, c-kit cells may confer structural and/or functional benefits primarily through paracrine biological activities. However, there are still conflicting hypotheses regarding how these paracrine effects work to improve cardiac function. While some authors suggested the promotion of cardiomyocyte renewal [73], others attributed it to new vessel formation [74,75].

5. Conclusions

This work presents a fully biodegradable, biomimetic epicardial patch (PGF), successfully developed and validated to promote endogenous myocardial repair by providing synergistic cues The incorporation of the conductive Fmoc-FF peptide not only reduced the patch's electrical impedance to a physiologically relevant level but also unexpectedly enhanced its microstructural stability and its ability to support cardiac cell alignment and function *in vitro*. The strength of this approach was confirmed in a preclinical model of myocardial infarction, where the PGF patch preserved cardiac tissue, reduced fibrosis, and promoted the recruitment of endogenous c-Kit+ cells. These findings demonstrate that our acellular, multi-faceted, patch effectively creates a pro-regenerative microenvironment for the damaged heart. This comprehensive study, spanning material design, *in vitro* validation, and *in vivo* efficacy, provides a strong foundation for future investigations. Building on these promising results, future work will aim to elucidate the precise molecular mechanisms by which the PGF patch activates epicardial cells and modulates the healing response. Demonstrating these functional benefits and evaluating the patch's long-term degradation profile, directly assessing its ability to enhance overall cardiac function in a clinically relevant large animal model will be the final steps toward translating this innovative therapeutic strategy to the clinic.

CRediT authorship contribution statement

Caterina Cristallini: Writing – review & editing, Writing – original draft, Validation, Supervision, Investigation, Funding acquisition, Data curation, Conceptualization. **Daniela Rossin:** Writing – review & editing, Writing – original draft, Visualization, Investigation, Formal analysis. **Niccoletta Barbani:** Writing – review & editing, Investigation, Formal analysis. **Roberto Vanni:** Writing – review & editing, Investigation, Formal analysis. **Massimiliano Labardi:** Writing – review & editing, Investigation, Formal analysis. **Cheherazade Trouki:** Writing – review & editing, Visualization, Investigation, Formal analysis. **Silvia Burchielli:** Writing – review & editing, Validation. **Claudia Kusmic:** Writing – review & editing, Validation, Investigation, Formal analysis. **Domiziana Terlizzi:** Validation. **Francesca Sergi:** Investigation, Formal analysis, Data curation. **Chiara Bulgheresi:** Investigation, Formal analysis, Data curation. **Dawid Rossino:** Writing – review &

editing, Investigation, Formal analysis. **Erika Fiorino:** Investigation. **Matteo Aubry:** Investigation. **Marco Lo Iacono:** Investigation. **Sadia Perveen:** Investigation, Formal analysis. **Giorgia Scarpellino:** Investigation, Formal analysis. **Luca Munaron:** Writing – review & editing, Formal analysis. **Sara Amorim:** Investigation. **Ricardo A. Pires:** Investigation, Formal analysis. **Rui L. Reis:** Funding acquisition. **Raffaella Rastaldo:** Writing – review & editing, Writing – original draft, Supervision, Funding acquisition, Conceptualization. **Claudia Giachino:** Writing – review & editing, Writing – original draft, Supervision, Funding acquisition, Data curation, Conceptualization.

Declaration of competing interest

Caterina Cristallini, Niccoletta Barbani, Massimiliano Labardi, Raffaella Rastaldo, Claudia Giachino, Ricardo Alexandre Pires, Sara Amorim, Rui Luis Reis, have patent pending to University of Turin and CNR of Pisa. The other authors declare that they have no known competing financial interests or personal relationships that could have appeared to influence the work reported in this paper.

Acknowledgements

This research study was supported by transnational EU project INCIPIT M-ERA.NET 2 call 2016, MIUR (DD n. 1218, 21/06/2019) FIRST; PoC Instrument-II cut-off 2020, Fondazione Compagnia di San Paolo (Compagnia di San Paolo Foundation); this work was also supported by the National Recovery and Resilience Plan (NRRP), Mission 4, Component 2, Investment 1.1, Call for tender No. 104 published on 2.2.2022 by the Italian Ministry of University and Research (MUR), funded by the European Union – NextGenerationEU – Project Title *Innovative development of a cardiac patch in the industrialization phase for the activation of regenerative and protective processes of cardiac ischemic tissues* – CUP D53D23013370006, B53D23020090006 – Grant Assignment Decree No. 2022ATB4TP. The authors acknowledge the contribution of Federico Alessandro Ruffinatti for assistance in electrophysiological experimental design; Rachele Rosso, Lelio Sciulli, and Emanuela Vitale for assistance in cellular and molecular analyses.

Appendix A. Supplementary data

Supplementary data to this article can be found online at https://doi.org/10.1016/j.bioadv.2025.214523.

Data availability

The data that support the findings of this study are available from the corresponding author upon reasonable request.

References

[1] M. Tajabadi, H. Goran Orimi, M.R. Ramzgouyan, A. Nemati, N. Deravi, N. Beheshtizadeh, M. Azami, Regenerative strategies for the consequences of myocardial infarction: chronological indication and upcoming visions, Biomed. Pharmacother. 146 (2022) 112584, https://doi.org/10.1016/j.biopha.2021.112584.

[2] M. Csöbönyeiová, N. Beerová, M. Klein, M. Debreová-Čeháková, Ľ. Danišovič, Cell-based and selected cell-free therapies for myocardial infarction: how do they compare to the current treatment options? Int. J. Mol. Sci. 23 (2022) 10314 https://doi.org/10.3390/ijms231810314.

[3] T.M. Maddox, J.L. Januzzi, L.A. Allen, K. Breathett, J. Butler, L.L. Davis, G. C. Fonarow, N.E. Ibrahim, J. Lindenfeld, F.A. Masoudi, S.R. Motiwala, E. Oliveros, J.H. Patterson, M.N. Walsh, A. Wasserman, C.W. Yancy, Q.R. Youmans, Update to the 2017 ACC expert consensus decision pathway for optimization of heart failure treatment: answers to 10 pivotal issues about heart failure with reduced ejection fraction, J. Am. Coll. Cardiol. 77 (2021) 772–810, https://doi.org/10.1016/j.jacc.2020.11.022.

[4] M. Isomi, T. Sadahiro, M. Ieda, Progress and challenge of cardiac regeneration to treat heart failure, J. Cardiol. 73 (2019) 97–101, https://doi.org/10.1016/j.jjcc.2018.10.002.

[5] S. Perveen, D. Rossin, E. Vitale, R. Rosso, R. Vanni, C. Cristallini, R. Rastaldo, C. Giachino, Therapeutic acellular scaffolds for limiting left ventricular remodelling-current status and future directions, Int. J. Mol. Sci. 22 (2021), https://doi.org/10.3390/ijms222313054.

[6] T. Liu, Y. Hao, Z. Zhang, H. Zhou, S. Peng, D. Zhang, K. Li, Y. Chen, M. Chen, Advanced cardiac patches for the treatment of myocardial infarction, Circulation 149 (2024) 2002–2020, https://doi.org/10.1161/CIRCULATIONAHA.123.067097.

[7] C.D. Roche, G.R. Iyer, M.H. Nguyen, S. Mabroora, A. Dome, K. Sakr, R. Pawar, V. Lee, C.C. Wilson, C. Gentile, Cardiac patch transplantation instruments for robotic minimally invasive cardiac surgery: initial proof-of-concept designs and surgery in a porcine cadaver, Front. Robot. AI 8 (2022) 714356, https://doi.org/10.3389/frobt.2021.714356.

[8] T. Hendrickson, C. Mancino, L. Whitney, C. Tsao, M. Rahimi, F. Taraballi, Mimicking cardiac tissue complexity through physical cues: a review on cardiac tissue engineering approaches, Nanomedicine 33 (2021) 102367, https://doi.org/10.1016/j.nano.2021.102367.

[9] S. Yang, K.-F. Leong, Z. Du, C.-K. Chua, The Design of Scaffolds for use in tissue engineering. Part I. Traditional factors, Tissue Eng. 7 (2001) 679–689, https://doi.org/10.1089/107632701753337645.

[10] C.F. Guimarães, L. Gasperini, A.P. Marques, R.L. Reis, The stiffness of living tissues and its implications for tissue engineering, Nat. Rev. Mater. 5 (2020) 351–370, https://doi.org/10.1038/s41578-019-0169-1.

[11] N. Goonoo, Tunable biomaterials for myocardial tissue regeneration: promising new strategies for advanced biointerface control and improved therapeutic outcomes, Biomater. Sci. 10 (2022) 1626–1646, https://doi.org/10.1039/D1BM01641E.

[12] Y. Xu, C. Kim, D.M. Saylor, D. Koo, Polymer degradation and drug delivery in <scp>PLGA</scp> −based drug–polymer applications: a review of experiments and theories, J Biomed Mater Res B Appl Biomater 105 (2017) 1692–1716, https://doi.org/10.1002/jbm.b.33648.

[13] C. Cristallini, E. Cibrario Rocchietti, L. Accomasso, A. Folino, C. Gallina, L. Muratori, P. Pagliaro, R. Rastaldo, S. Raimondo, S. Saviozzi, A.E. Sprio, M. Gagliardi, N. Barbani, C. Giachino, The effect of bioartificial constructs that mimic myocardial structure and biomechanical properties on stem cell commitment towards cardiac lineage, Biomaterials 35 (2014) 92–104, https://doi.org/10.1016/j.biomaterials.2013.09.058.

[14] K.D. Dwyer, K.L.K. Coulombe, Cardiac mechanostructure: using mechanics and anisotropy as inspiration for developing epicardial therapies in treating myocardial infarction, Bioact Mater 6 (2021) 2198–2220, https://doi.org/10.1016/j.bioactmat.2020.12.015.

[15] D.-H. Kim, E.A. Lipke, P. Kim, R. Cheong, S. Thompson, M. Delannoy, K.-Y. Suh, L. Tung, A. Levchenko, Nanoscale cues regulate the structure and function of macroscopic cardiac tissue constructs, Proc. Natl. Acad. Sci. 107 (2010) 565–570, https://doi.org/10.1073/pnas.0906504107.

[16] C. Cristallini, E. Cibrario Rocchietti, M. Gagliardi, L. Mortati, S. Saviozzi, E. Bellotti, V. Turinetto, M.P. Sassi, N. Barbani, C. Giachino, Micro- and macrostructured PLGA/gelatin scaffolds promote early cardiogenic commitment of human mesenchymal stem cells in vitro, Stem Cells Int. 2016 (2016) 1–16, https://doi.org/10.1155/2016/7176154.

[17] C. Cristallini, G. Vaccari, N. Barbani, E. Cibrario Rocchietti, R. Barberis, M. Falzone, K. Cabiale, G. Perona, E. Bellotti, R. Rastaldo, S. Pascale, P. Pagliaro, C. Giachino, Cardioprotection of PLGA/gelatine cardiac patches functionalised with adenosine in a large animal model of ischaemia and reperfusion injury: a feasibility study, J. Tissue Eng. Regen. Med. 13 (2019) 1253–1264, https://doi.org/10.1002/term.2875.

[18] H. Esmaeili, A. Patino-Guerrero, M. Hasany, M.O. Ansari, A. Memic, A. Dolatshahi-Pirouz, M. Nikkhah, Electroconductive biomaterials for cardiac tissue engineering, Acta Biomater. 139 (2022) 118–140, https://doi.org/10.1016/j.actbio.2021.08.031.

[19] M. Morsink, P. Severino, E. Luna-Ceron, M.A. Hussain, N. Sobahi, S.R. Shin, Effects of electrically conductive nano-biomaterials on regulating cardiomyocyte behavior for cardiac repair and regeneration, Acta Biomater. 139 (2022) 141–156, https://doi.org/10.1016/j.actbio.2021.11.022.

[20] S. Saravanan, N. Sareen, E. Abu-El-Rub, H. Ashour, G.L. Sequiera, H.I. Ammar, V. Gopinath, A.A. Shamaa, S.S.E. Sayed, M. Moudgil, J. Vadivelu, S. Dhingra, Graphene oxide-gold nanosheets containing chitosan scaffold improves ventricular contractility and function after implantation into infarcted heart, Sci. Rep. 8 (2018) 15069, https://doi.org/10.1038/s41598-018-33144-0.

[21] Z. Liu, S.M. Tabakman, Z. Chen, H. Dai, Preparation of carbon nanotube bioconjugates for biomedical applications, Nat. Protoc. 4 (2009) 1372–1381, https://doi.org/10.1038/nprot.2009.146.

[22] R. Balint, N.J. Cassidy, S.H. Cartmell, Conductive polymers: towards a smart biomaterial for tissue engineering, Acta Biomater. 10 (2014) 2341–2353, https://doi.org/10.1016/j.actbio.2014.02.015.

[23] P. Shokrollahi, Y. Omidi, L.X. Cubeddu, H. Omidian, Conductive polymers for cardiac tissue engineering and regeneration, J Biomed Mater Res B Appl Biomater 111 (2023) 1979–1995, https://doi.org/10.1002/jbm.b.35293.

[24] A. Chen, H. Brand, T. Helbig, T. Hofmann, S. Imhof, A. Fritzsche, T. Kießling, A. Stegmaier, L.K. Upreti, T. Neupert, T. Bzdušek, M. Greiter, R. Thomale, I. Boettcher, Hyperbolic matter in electrical circuits with tunable complex phases, Nat. Commun. 14 (2023) 622, https://doi.org/10.1038/s41467-023-36359-6.

[25] L. Wang, Y. Liu, G. Ye, Y. He, B. Li, Y. Guan, B. Gong, K. Mequanint, M.M.Q. Xing, X. Qiu, Injectable and conductive cardiac patches repair infarcted myocardium in rats and minipigs, Nat. Biomed. Eng. 5 (2021) 1157–1173, https://doi.org/10.1038/s41551-021-00796-9.

[26] J. Dai, B. Wang, Z. Chang, X. Lu, J. Nie, Q. Ren, Y. Lv, M.Y. Rotenberg, Y. Fang, Injectable mesh-like conductive hydrogel patch for elimination of atrial fibrillation, Adv. Healthc. Mater. 13 (2024), https://doi.org/10.1002/adhm.202303219.

[27] L. Zhao, Z. Chang, B. Guo, Y. Lu, X. Lu, Q. Ren, A. Lv, J. Nie, D. Ji, M.Y. Rotenberg, B. Wang, Y. Zhang, Y. Fang, Robust, stretchable bioelectronic interfaces for cardiac pacing enabled by interfacial transfer of laser-induced graphene via water-response, nonswellable PVA gels, Biosens. Bioelectron. 261 (2024) 116453, https://doi.org/10.1016/j.bios.2024.116453.
[28] Q. Xu, Z. Xiao, Q. Yang, T. Yu, X. Deng, N. Chen, Y. Huang, L. Wang, J. Guo, J. Wang, Hydrogel-based cardiac repair and regeneration function in the treatment of myocardial infarction, Mater. Today Bio 25 (2024) 100978, https://doi.org/10.1016/j.mtbio.2024.100978.
[29] K. Roshanbinfar, M. Schiffer, E. Carls, M. Angeloni, M. Koleśnik-Gray, S. Schruefer, D.W. Schubert, F. Ferrazzi, V. Krstić, B.K. Fleischmann, W. Roell, F.B. Engel, Electrically conductive collagen-PEDOT:PSS hydrogel prevents post-infarct cardiac arrhythmia and supports hiPSC-cardiomyocyte function, Adv. Mater. 36 (2024), https://doi.org/10.1002/adma.202403642.
[30] M. Lee, M.C. Kim, J.Y. Lee, Nanomaterial-based electrically conductive hydrogels for cardiac tissue repair, Int. J. Nanomedicine 17 (2022) 6181–6200, https://doi.org/10.2147/IJN.S386763.
[31] C. Yu, M. Shi, S. He, M. Yao, H. Sun, Z. Yue, Y. Qiu, B. Liu, L. Liang, Z. Zhao, F. Yao, H. Zhang, J. Li, Chronological adhesive cardiac patch for synchronous mechanophysiological monitoring and electrocoupling therapy, Nat. Commun. 14 (2023) 6226, https://doi.org/10.1038/s41467-023-42008-9.
[32] M. Solazzo, F.J. O'Brien, V. Nicolosi, M.G. Monaghan, The rationale and emergence of electroconductive biomaterial scaffolds in cardiac tissue engineering, APL Bioeng. 3 (2019), https://doi.org/10.1063/1.5116579.
[33] B. Guo, L. Glavas, A.-C. Albertsson, Biodegradable and electrically conducting polymers for biomedical applications, Prog. Polym. Sci. 38 (2013) 1263–1286, https://doi.org/10.1016/j.progpolymsci.2013.06.003.
[34] Y. Wang, Q. Geng, Y. Zhang, L. Adler-Abramovich, X. Fan, D. Mei, E. Gazit, K. Tao, Fmoc-diphenylalanine gelating nanoarchitectonics: a simplistic peptide self-assembly to meet complex applications, J. Colloid Interface Sci. 636 (2023) 113–133, https://doi.org/10.1016/j.jcis.2022.12.166.
[35] A. Mahler, M. Reches, M. Rechter, S. Cohen, E. Gazit, Rigid, self-assembled hydrogel composed of a modified aromatic dipeptide, Adv. Mater. 18 (2006) 1365–1370, https://doi.org/10.1002/adma.200501765.
[36] V. Jayawarna, M. Ali, T.A. Jowitt, A.F. Miller, A. Saiani, J.E. Gough, R.V. Ulijn, Nanostructured hydrogels for three-dimensional cell culture through self-assembly of fluorenylmethoxycarbonyl–dipeptides, Adv. Mater. 18 (2006) 611–614, https://doi.org/10.1002/adma.200501522.
[37] M. Zhou, R.V. Ulijn, J.E. Gough, Extracellular matrix formation in self-assembled minimalistic bioactive hydrogels based on aromatic peptide amphiphiles, J. Tissue Eng. 5 (2014), https://doi.org/10.1177/2041731414531593.
[38] A. Brito, Y.M. Abul-Haija, D.S. da Costa, R. Novoa-Carballal, R.L. Reis, R.V. Ulijn, R.A. Pires, I. Pashkuleva, Minimalistic supramolecular proteoglycan mimics by co-assembly of aromatic peptide and carbohydrate amphiphiles, Chem. Sci. 10 (2019) 2385–2390, https://doi.org/10.1039/C8SC04361B.
[39] X. Gong, C. Branford-White, L. Tao, S. Li, J. Quan, H. Nie, L. Zhu, Preparation and characterization of a novel sodium alginate incorporated self-assembled Fmoc-FF composite hydrogel, Mater. Sci. Eng. C 58 (2016) 478–486, https://doi.org/10.1016/j.msec.2015.08.059.
[40] Y. Wang, S. Lin, S.R. Nelli, F. Zhan, H. Cheng, T. Lai, M. Yeh, H. Lin, S. Hung, Self-assembled peptide-based hydrogels as scaffolds for proliferation and multi-differentiation of mesenchymal stem cells, Macromol. Biosci. 17 (2017), https://doi.org/10.1002/mabi.201600192.
[41] V.I.B. Castro, S. Amorim, D. Caballero, C.M. Abreu, S.C. Kundu, R.L. Reis, I. Pashkuleva, R.A. Pires, Patterned glycopeptide-based supramolecular hydrogel promotes the alignment and contractility of iPSC-derived cardiomyocytes, Biomater. Adv. 167 (2025) 214091, https://doi.org/10.1016/j.bioadv.2024.214091.
[42] F. Fouladgar, F.G. Zadeh Moslabeh, Y.V. Kasani, N. Rogozinski, M. Torres, M. Ecker, H. Yang, Y. Yang, N. Habibi, Mesenchymal stem cells aligned and stretched in self-assembling peptide hydrogels, Heliyon 10 (2024) e23953, https://doi.org/10.1016/j.heliyon.2023.e23953.
[43] E. Vitale, R. Rosso, M. Lo Iacono, C. Cristallini, C. Giachino, R. Rastaldo, Apelin-13 increases functional Connexin-43 through autophagy inhibition via AKT/mTOR pathway in the non-myocytic cell population of the heart, Int. J. Mol. Sci. 23 (2022) 13073, https://doi.org/10.3390/ijms232113073.
[44] F. Forini, C. Kusmic, G. Nicolini, L. Mariani, R. Zucchi, M. Matteucci, G. Iervasi, L. Pitto, Triiodothyronine prevents cardiac ischemia/reperfusion mitochondrial impairment and cell loss by regulating miR30a/p53 axis, Endocrinology 155 (2014) 4581–4590, https://doi.org/10.1210/en.2014-1106.
[45] R. Bao, B. Tan, S. Liang, N. Zhang, W. Wang, W. Liu, A π-π conjugation-containing soft and conductive injectable polymer hydrogel highly efficiently rebuilds cardiac function after myocardial infarction, Biomaterials 122 (2017) 63–71, https://doi.org/10.1016/j.biomaterials.2017.01.012.
[46] Q.-Z. Chen, S.E. Harding, N.N. Ali, A.R. Lyon, A.R. Boccaccini, Biomaterials in cardiac tissue engineering: ten years of research survey, Mater. Sci. Eng. R. Rep. 59 (2008) 1–37, https://doi.org/10.1016/j.mser.2007.08.001.
[47] S. Ramadan, N. Paul, H.E. Naguib, Standardized static and dynamic evaluation of myocardial tissue properties, Biomed. Mater. 12 (2017) 025013, https://doi.org/10.1088/1748-605X/aa57a5.
[48] J. Lennartsson, L. Rönnstrand, Stem cell factor receptor/c-kit: from basic science to clinical implications, Physiol. Rev. 92 (2012) 1619–1649, https://doi.org/10.1152/physrev.00046.2011.
[49] S.S. Razzaq, I. Khan, N. Naeem, A. Salim, S. Begum, K. Haneef, Overexpression of GATA binding protein 4 and myocyte enhancer factor 2C induces differentiation of mesenchymal stem cells into cardiac-like cells, World J. Stem Cells 14 (2022) 700–713, https://doi.org/10.4252/wjsc.v14.i9.700.
[50] A. Piasecka, M. Sekrecki, M.W. Szcześniak, K. Sobczak, MEF2C shapes the microtranscriptome during differentiation of skeletal muscles, Sci. Rep. 11 (2021) 3476, https://doi.org/10.1038/s41598-021-82706-2.
[51] C. Cao, L. Li, Q. Zhang, H. Li, Z. Wang, A. Wang, J. Liu, Nkx2.5: a crucial regulator of cardiac development, regeneration and diseases, Front. Cardiovasc. Med. 10 (2023), https://doi.org/10.3389/fcvm.2023.1270951.
[52] U. Chalise, M. Becirovic-Agic, M.L. Lindsey, The cardiac wound healing response to myocardial infarction, WIREs Mech. Dis. 15 (2023), https://doi.org/10.1002/wsbm.1584.
[53] P. Baei, S. Jalili-Firoozinezhad, S. Rajabi-Zeleti, M. Tafazzoli-Shadpour, H. Baharvand, N. Aghdami, Electrically conductive gold nanoparticle-chitosan thermosensitive hydrogels for cardiac tissue engineering, Mater. Sci. Eng. C 63 (2016) 131–141, https://doi.org/10.1016/j.msec.2016.02.056.
[54] K. Tao, P. Makam, R. Aizen, E. Gazit, Self-assembling peptide semiconductors, Science (1979) 358 (2017), https://doi.org/10.1126/science.aam9756.
[55] N.P. Reynolds, Amyloid-like peptide nanofibrils as scaffolds for tissue engineering: progress and challenges (review), Biointerphases 14 (2019), https://doi.org/10.1116/1.5098332.
[56] Y. Liang, A. Mitriashkin, T.T. Lim, J.C.-H. Goh, Conductive polypyrrole-encapsulated silk fibroin fibers for cardiac tissue engineering, Biomaterials 276 (2021) 121008, https://doi.org/10.1016/j.biomaterials.2021.121008.
[57] C. Mancino, T. Hendrickson, L.V. Whitney, F. Paradiso, S. Abasi, E. Tasciotti, F. Taraballi, A. Guiseppi-Elie, Electrospun electroconductive constructs of aligned fibers for cardiac tissue engineering, Nanomedicine 44 (2022) 102567, https://doi.org/10.1016/j.nano.2022.102567.
[58] J.G. Stinstra, B. Hopenfeld, R.S. MacLeod, On the passive cardiac conductivity, Ann. Biomed. Eng. 33 (2005) 1743–1751, https://doi.org/10.1007/s10439-005-7257-7.
[59] M.I. Echeverria Molina, K.G. Malollari, K. Komvopoulos, Design challenges in polymeric scaffolds for tissue engineering, Front. Bioeng. Biotechnol. 9 (2021), https://doi.org/10.3389/fbioe.2021.617141.
[60] M. Modrák, M. Trebuňová, A.F. Balogová, R. Hudák, J. Živčák, Biodegradable materials for tissue engineering: development, classification and current applications, J. Funct. Biomater. 14 (2023) 159, https://doi.org/10.3390/jfb14030159.
[61] S.H. Pujari, S. Sharma, P. Agasthi, Left Ventricular Rupture, 2024.
[62] A. Gelmi, A. Cieslar-Pobuda, E. de Muinck, M. Los, M. Rafat, E.W.H. Jager, Direct mechanical stimulation of stem cells: a beating electromechanically active scaffold for cardiac tissue engineering, Adv. Healthc. Mater. 5 (2016) 1471–1480, https://doi.org/10.1002/adhm.201600307.
[63] H.S. Yang, B. Lee, J.H. Tsui, J. Macadangdang, S. Jang, S.G. Im, D. Kim, Electroconductive nanopatterned substrates for enhanced myogenic differentiation and maturation, Adv. Healthc. Mater. 5 (2016) 137–145, https://doi.org/10.1002/adhm.201500003.
[64] L. Wang, Y. Wu, T. Hu, B. Guo, P.X. Ma, Electrospun conductive nanofibrous scaffolds for engineering cardiac tissue and 3D bioactuators, Acta Biomater. 59 (2017) 68–81, https://doi.org/10.1016/j.actbio.2017.06.036.
[65] Y. Zhang, A. Le Friec, M. Chen, 3D anisotropic conductive fibers electrically stimulated myogenesis, Int. J. Pharm. 606 (2021) 120841, https://doi.org/10.1016/j.ijpharm.2021.120841.
[66] A.-D. Bendrea, L. Cianga, I. Cianga, Review paper: progress in the field of conducting polymers for tissue engineering applications, J. Biomater. Appl. 26 (2011) 3–84, https://doi.org/10.1177/0885328211402704.
[67] S. Rohr, Role of gap junctions in the propagation of the cardiac action potential, Cardiovasc. Res. 62 (2004) 309–322, https://doi.org/10.1016/j.cardiores.2003.11.035.
[68] N.J. Severs, A.F. Bruce, E. Dupont, S. Rothery, Remodelling of gap junctions and connexin expression in diseased myocardium, Cardiovasc. Res. 80 (2008) 9–19, https://doi.org/10.1093/cvr/cvn133.
[69] F. Di Meglio, C. Castaldo, D. Nurzynska, V. Romano, R. Miraglia, C. Bancone, G. Langella, C. Vosa, S. Montagnani, Epithelial–mesenchymal transition of epicardial mesothelium is a source of cardiac CD117-positive stem cells in adult human heart, J. Mol. Cell. Cardiol. 49 (2010) 719–727, https://doi.org/10.1016/j.yjmcc.2010.05.013.
[70] C. Castaldo, F. Di Meglio, D. Nurzynska, G. Romano, C. Maiello, C. Bancone, P. Müller, M. Böhm, M. Cotrufo, S. Montagnani, CD117-positive cells in adult human heart are localized in the subepicardium, and their activation is associated with laminin-1 and α6 integrin expression, Stem Cells 26 (2008) 1723–1731, https://doi.org/10.1634/stemcells.2007-0732.
[71] F. Di Meglio, C. Castaldo, D. Nurzynska, R. Miraglia, V. Romano, V. Russolillo, L. Giuseppina, C. Vosa, S. Montagnani, Localization and origin of cardiac CD117-positive cells: identification of a population of epicardially-derived cells in adult human heart, Ital. J. Anat. Embryol. 115 (2010) 71–78.
[72] M.C.L. Keith, R. Bolli, "String theory" of c-kit ^{pos} cardiac cells, Circ. Res. 116 (2015) 1216–1230, https://doi.org/10.1161/CIRCRESAHA.116.305557.
[73] T. Eschenhagen, R. Bolli, T. Braun, L.J. Field, B.K. Fleischmann, J. Frisén, M. Giacca, J.M. Hare, S. Houser, R.T. Lee, E. Marbán, J.F. Martin, J.D. Molkentin, C.E. Murry, P.R. Riley, P. Ruiz-Lozano, H.A. Sadek, M.A. Sussman, J.A. Hill,

Cardiomyocyte regeneration, Circulation 136 (2017) 680–686, https://doi.org/10.1161/CIRCULATIONAHA.117.029343.
[74] S. Xing, J.-Z. Tian, S.-H. Yang, X.-T. Huang, Y.-F. Ding, Q.-Y. Lu, J.-S. Yang, W.-J. Yang, Setd4 controlled quiescent c-Kit+ cells contribute to cardiac neovascularization of capillaries beyond activation, Sci. Rep. 11 (2021) 11603, https://doi.org/10.1038/s41598-021-91105-6.
[75] J.H. van Berlo, O. Kanisicak, M. Maillet, R.J. Vagnozzi, J. Karch, S.-C.J. Lin, R. C. Middleton, E. Marbán, J.D. Molkentin, c-kit+ cells minimally contribute cardiomyocytes to the heart, Nature 509 (2014) 337–341, https://doi.org/10.1038/nature13309.